class C low-molecular-weight PBPs *E. coli* PBP4,[40] *B. subtilis* PBP4a, *Actinomadura* R39 DD-peptidase,[41,42] and *E. coli* PBP5.[43,44] This hypothesis is supported by the recently solved X-ray crystal structure of *Actinomadura* R39 DD-peptidase in complex with a cephalosporin bearing a peptidoglycan mimetic side chain.[45] This model shows specific interactions between the ammonium carboxylate group of *meso*-2,6-diaminopimelic acid and a subsite composed of Asp142, Tyr147, Arg351, and Ser415 (*Actinomadura* R39 numbering). SA-PBP3 has no equivalent residues, and the space between residues 424–427 and 621–623 is comparatively wide.

Despite the presence of the so-called dimerization domain within the sequence and an apparently tight dimer interface formed by β-strands elsewhere in the N-domain, the protein shows no tendency to associate in solution. SA-PBP3 appears to be a cautionary example showing that bioinformatics tools alone are unreliable predictors of protein structure and association. The dimer interface revealed by the crystal structure may be relevant *in vivo*, possibly as part of a larger protein complex, with PBP3 attached to the cell membrane at its N-terminus. Since the N-terminal region of each subunit faces the same direction, attachment of each subunit to the membrane does not preclude dimer formation. The fact that PBP3 deletion mutants grow better than wild-type *S. aureus* under conditions where PBP3 is inhibited suggests that the protein associates into a heterocomplex that operates better without PBP3 than with inactive PBP3.[12] The nature of such a complex is presently unclear.

Materials and Methods

Cloning, expression, and purification of PBP3

The PBP3 gene was amplified by PCR using cloned cDNA (*S. aureus*/MW2) obtained from the National Institute of Technology and Evaluation. The primers used were 5′-GGGCCCGGATCCCAAGGCTCACATTATAAACAAATTATAAA-3′ and 5′-GGGCCCGCGGCCGCCGCGCGTTATTTGTCTTTGTCTTTATTT-3′.

The product, encoding PBP3 residues 46–691, was digested with BamHI and NotI and then ligated into suitably cut modified pET28b vector, in which a Shine–Dalgarno sequence, an initial ATG, a hexa-histidine tag, and a tobacco etch virus (TEV) protease cleavage site had been cloned between XbaI and BamHI restriction sites. The pET28b/PBP3 plasmid was transformed into *E. coli* BL21(DE3). Cells were grown at 37 °C in LB medium containing 50 μg/ml kanamycin up to OD_{600} between 0.6 and 0.8. Protein expression was induced by adding IPTG to a final concentration of 0.5 mM and incubating the culture with shaking at 15 °C overnight. After harvesting by centrifugation at 4000*g* for 15 min, we resuspended cells in Ni-NTA binding buffer [20 mM Tris (pH 8.0), 500 mM NaCl, 500 mM urea, 25 mM imidazole, and 10 mM 2-mercaptoethanol] and lysed by sonication. After centrifugation at 40,000*g* for 30 min, the supernatant was loaded onto a 20-ml Ni-NTA Sepharose column (QIAGEN) equilibrated with the same buffer. Protein was eluted by a 25- to 500-mM linear gradient of imidazole. Peak fractions were collected, and His tag was removed with 0.2 μM His-tagged TEV protease at room temperature while dialyzing for overnight against Ni-NTA binding buffer. The molar ratio of PBP3 to TEV protease was 10:1. Protein was reloaded onto the same Ni-NTA Sepharose column to remove His-tagged protein, including TEV protease, and minor protein contaminants. The fractions containing PBP3 were dialyzed against SP binding buffer [20 mM sodium phosphate (pH 6.0) and 100 mM NaCl] and were loaded onto SP-Sepharose (GE Healthcare) equilibrated with the same buffer. Protein was eluted using a linear gradient of 100–1000 mM NaCl. The peak fractions were directly loaded onto a hydroxyapatite column (Bio-Rad) and eluted with a 20- to 1000-mM linear gradient of potassium phosphate (pH 6.0). Finally, protein was dialyzed overnight against crystallization buffer [20 mM Tris–HCl (pH 8.0) and 100 mM NaCl] and passed through Q-Sepharose (GE Healthcare) to separate off minor protein and nucleic acid contaminants. The sample was concentrated to 20 mg/ml by ultrafiltration using a Centriprep YM-30 (Millipore).

Mutagenesis

Site-directed mutagenesis replacing Ser392 to alanine was carried out with a simple PCR procedure. The regions encoding residues 46–392 and 392–691 were amplified using the following pairs of forward and reverse primers, respectively:
5′-GGGCCCGGATCCCAAGGCTCACATTATAAACAAATTATAAA-3′ with 5′-GCTAATAATGTTCCACCTTTTACAGAAGCTCCAACCGCAAATTGAGAAGTAAACGTACC-3′ for the N-terminal region and 5′-GGTACGTTTACTTCTCAATTTGCGGTTGGAGCTTCTGTAAAAGGTGGAACATTATTAGC-3′ with 5′-GGGCCCGCGGCCGCCGCGCGTTATTTGTCTTTGTCTTTATTT-3′ for the C-terminal region. The reverse primer for the N-terminal region is the reverse complement of the forward primer for the C-terminal region. The purified overlapping fragments were joined together and amplified by PCR and then treated with BamHI and NotI. The fragment was ligated into suitably cut modified pET28b vector. Mutant protein was expressed and purified using the same protocol as for the wild type.

Crystallization

PBP3 was crystallized by the vapor diffusion hanging-drop method. Drops were formed by mixing 1.5 μl of protein solution with 1.5 μl of reservoir solution, then equilibrated against 500 μl of reservoir solution at 20 °C. Crystals of native and Se-Met PBP3 were grown in 2.0 M AmSO4, 0.5 M LiCl, and 5% (v/v) glycerol and 1.8 M AmSO4 and 0.4 M $NaNO_3$, respectively. For heavy-atom derivatization, crystals were soaked in reservoir solution containing 0.5 mM thimerosal (Hg) or 0.5 mM K_2PtCl_4 for 12 h before data collection. Crystals formed in the space

Table 1. Statistics of the crystallographic analysis

	Native	Cefotaxime	Se-Met	Hg	Pt
Data sets					
Space group	$P4_32_12$				
Unit cell					
a, *b*, *c* (Å)	143.4, 143.4, 189.4	143.0, 143.0, 189.6	143.4, 143.4, 189.6	142.8, 142.8, 190.6	142.4, 142.4, 190.4
Resolution range (Å)	50.0–2.3	50.0–2.4	20.0–2.9	50.0–3.2	50.0–3.3
Reflections (measured/unique)	483,661/85,132	431,478/76,011	845,441/43,698	484,063/33,363	427,946/30,123
Completeness (overall/outer shell, %)[a]	96.7/89.4	98.2/89.0	97.8/80.0	100/100	100/99.0
R_{merge} (overall/outer shell, %)[a]	9.0/49.4	11.1/46.0	11.7/39.5	10.5/51.5	10.2/56.1
Redundancy (overall/outer shell)	5.7/3.0	5.7/2.3	19.3/4.0	14.5/14.8	14.2/14.5
Mean $\langle I/\sigma(I)\rangle$ (overall/outer shell)	15.9/1.5	11.4/1.4	24.2/1.8	38.1/7.6	45.9/7.4
Overall *B*-factor from Wilson plot (Å^2)	35.0	31.8	62.2	84.2	98.0
Metal sites			19	5	10
Phasing (20.0–2.3 Å)					
Mean FOM[b] after SHARP phasing (acentric/centric)			0.831/0.767	0.369/0.377	0.230/0.270
Refinement statistics					
Resolution range (Å)	50.0–2.3	50.0–2.4			
R-factor[c]/R_{free} (%)[c]	26.0/30.0	25.2/31.0			
rmsd bond lengths (Å)/bond angles (°)	0.010/1.461	0.010/1.465			
Number of water molecules	260	306			
Average *B*-factor (PBP3/water/ligand, Å^2)	77/51	69/45/103			
Ramachandran plot (%)					
Residues in most favorable regions	82.0	81.3			
Residues in additional allowed regions	16.9	17.4			
Residues in generously allowed regions	1.1	1.3			
Residues in disallowed regions	0	0			

The highest-resolution shells from left to right are 2.38–2.30, 2.44–2.40, 3.00–2.90, 3.31–3.20, and 3.42–3.30 Å, respectively.

[a] Completeness and R_{merge} are given for the overall data and for the highest-resolution shell.

[b] Figure of merit (FOM)= $|Fbest| - |F|$.

[c] $R_{merge}=\sum|I_i-\langle I\rangle|/\sum|I_i|$, where I_i is the intensity of an observation and $\langle I\rangle$ is the intensity in the mean value for that reflection, and the summations are over all equivalents. *R*-factor= $\sum h||F_o(h)|-|F_c(h)||/\sum hF_o(h)$, where F_o and F_c are the observed and calculated structure factor amplitudes, respectively. R_{free} was calculated with 5% of the data excluded from the refinement.

group $P4_32_12$, with $a=b=143.4$ Å and $c=189.3$ Å and contained two molecules per asymmetric unit. Diffraction data were collected at −180 °C using crystals flash-frozen in crystallization buffer containing 17.5% (v/v) glycerol and 2.5% (v/v) dimethyl sulfoxide. Diffraction data from a native crystal were collected at 0.9 Å on beamline BL44XU stations at the SPring8, Harima, Japan, using a MX225HE detector. Derivative data were collected at 0.97909 Å (for Se-Met) and 1.0 Å (for Hg and Pt) on beamline BL17A stations at the Photon Factory, Tsukuba, Japan, using an ADSC Quantum 315 CCD detector. Crystals of the antibiotic complex were prepared by dissolving cefotaxime sodium salt (Wako) in the reservoir solution to 5 mM concentration and then adding 0.4 µl of this solution directly to the hanging drops containing protein crystals. Soaking was carried out for 12 h at 20 °C. Diffraction data were collected at 1.0 Å on beamline PF-BL1A at the Photon Factory. All data were processed and scaled using HKL2000 and scaled with SCALEPACK.[46]

Structure determination and refinement

The native and derivative data sets were used for phasing by MIR (*m*ultiple *i*somorphous *r*eplacement) using SHELXD[47] and Auto-SHARP.[48] Se-Met, platinum, and mercury sites and initial phases were determined using SHELXD. Solvent flattening using SOLOMON[49] in Auto-SHARP was used to improve phases. After density modification, an electron density map was calculated to a resolution of 2.3 Å. The map was of good quality, allowing much of the main chain to be traced. Successive rounds of model building were carried out using Coot[50]; refinement, using both REFMAC5[51] and PHENIX.[25] After an initial round of simulated annealing refinement, several macrocycles that included bulk solvent correction and anisotropic scaling of the data, individual coordinate refinement with minimization, and individual isotropic atomic displacement parameter refinement were carried out with maximum likelihood as the target. Non-crystallographic symmetry restraints were not applied. In the course of the refinement, water molecules were added to the models by manual inspection of their positions in both $2F_o-F_c$ and F_o-F_c maps, and combined TLS (*T*ranslation/*L*ibration/*S*crew) and individual atomic displacement parameter refinement were carried out in the final stages. The stereochemistry of the final model was assessed using Coot. Data collection and refinement statistics are shown in Table 1.

Analytical ultracentrifugation

The molecular weight and self-association of PBP3 in solution were examined using a Beckman Optima XL-1 analytical ultracentrifuge. The experiments were performed

at 20 °C, and absorbance at 280 nm was measured. Before the experiment, the sample was diluted to 10 μM with crystallization buffer. After thermal equilibration at rest for 2 h, sedimentation velocity data were measured at 50,000 rpm for 6 h and analyzed using SEDFIT version 9.4.[52]

NanoESI mass spectrometry

Nanoelectrospray ionization (nanoESI) mass spectra of free and ligand-bound PBP3 were obtained by Q-Tof-2 (Waters, Milford, MA) with a nanoelectrospray ion source. To observe the native state of free PBP3 in solution, we prepared the PBP3 samples by dialysis against 100 mM ammonium acetate. The final concentration of PBP3 was estimated to be ~20 μM. PBP3 wild type and S392A mutant were mixed with antibiotic at a 1:1 molar ratio, dialyzed against 5 mM ammonium acetate, and diluted with 0.1% formic acid in 50% acetonitrile to make the final concentration to be ~10 μM in order to determine the masses of the ligand-bound forms more accurately.

An aliquot of 4 μl of each sample solution was placed in a HUMANIX nanoESI tip (Hiroshima, Japan) and electrosprayed with an applied capillary voltage of 1.0 kV. The pressure in the quadrupole ion guide of Q-Tof-2 was controlled by throttling down the Speedivalve fitted to the rotary pump if necessary. Each mass spectrum was acquired in 4 s, and more than 10 spectra were accumulated and smoothed with the Savitzky–Golay method. The program MaxEnt3 was used to deconvolute the original nanoESI mass spectra and determine the molecular masses of the ligand-bound forms.

Accession numbers

The models have been deposited in the Research Collaboratory for Structural Bioinformatics Protein Data Bank (PDB) with accession codes 3VSK (apo PBP3) and 3VSL (PBP3 with cefotaxime).

Acknowledgements

We thank staff at beamlines BL44XU and BL1A at SPring8 and the Photon Factory for assistance with data collection. S.-Y.P. is supported in part by the ISS Applied Research Partnership Program, Maura Foods and Biosciences Inc., and Confocal Science Inc. This work was supported in part by the Medical Research Council grants G0400848 and G500643 to D.I.R. and grants-in-aid from the Ministry of Education, Culture, Sports, Science and Technology of Japan to J.R.H.T.

References

1. Vollmer, W., Blanot, D. & de Pedro, M. A. (2008). Peptidoglycan structure and architecture. *FEMS Microbiol. Rev.* **32**, 149–167.
2. Sauvage, E., Kerff, F., Terrak, M., Ayala, J. A. & Charlier, P. (2008). The penicillin-binding proteins: structure and role in peptidoglycan biosynthesis. *FEMS Microbiol. Rev.* **32**, 234–258.
3. Ubukata, K., Nonoguchi, R., Matsuhashi, M. & Konno, M. (1989). Expression and inducibility in *Staphylococcus aureus* of the *mecA* gene, which encodes a methicillin-resistant *S. aureus*-specific penicillin-binding protein. *J. Bacteriol.* **171**, 2882–2885.
4. Morell, E. A. & Balkin, D. M. (2010). Methicillin-resistant *Staphylococcus aureus*: a pervasive pathogen highlights the need for new antimicrobial development. *Yale J. Biol. Med.* **83**, 223–233.
5. Banerjee, R., Gretes, M., Harlem, C., Basuino, L. & Chambers, H. F. (2010). A *mecA*-negative strain of methicillin-resistant *Staphylococcus aureus* with high-level β-lactam resistance contains mutations in three genes. *Antimicrob. Agents Chemother.* **54**, 4900–4902.
6. Tipper, D. J. & Strominger, J. L. (1965). Mechanism of action of penicillins: a proposal based on their structural similarity to acyl-D-alanyl-D-alanine. *Proc. Natl Acad. Sci. USA*, **54**, 1133–1141.
7. Contreras-Martel, C., Dahout-Gonzalez, C., Martins Ados, S., Kotnik, M. & Dessen, A. (2009). PBP active site flexibility as the key mechanism for β-lactam resistance in pneumococci. *J. Mol. Biol.* **387**, 899–909.
8. Goffin, C. & Ghuysen, J. M. (1998). Multimodular penicillin-binding proteins: an enigmatic family of orthologs and paralogs. *Microbiol. Mol. Biol. Rev.* **62**, 1079–1093.
9. Ghosh, A. S., Chowdhury, C. & Nelson, D. E. (2008). Physiological functions of D-alanine carboxypeptidases in *Escherichia coli*. *Trends Microbiol.* **16**, 309–317.
10. Memmi, G., Filipe, S. R., Pinho, M. G., Fu, Z. & Cheung, A. (2008). *Staphylococcus aureus* PBP4 is essential for β-lactam resistance in community-acquired methicillin-resistant strains. *Antimicrob. Agents Chemother.* **52**, 3955–3966.
11. Navratna, V., Nadig, S., Sood, V., Prasad, K., Arakere, G. & Gopal, B. (2010). Molecular basis for the role of *Staphylococcus aureus* penicillin binding protein 4 in antimicrobial resistance. *J. Bacteriol.* **192**, 134–144.
12. Pinho, M. G., de Lencastre, H. & Tomasz, A. (2000). Cloning, characterization, and inactivation of the gene *pbpC*, encoding penicillin-binding protein 3 of *Staphylococcus aureus*. *J. Bacteriol.* **182**, 1074–1079.
13. Fraipont, C., Alexeeva, S., Wolf, B., van der Ploeg, R., Schloesser, M., den Blaauwen, T. & Nguyen-Disteche, M. (2011). The integral membrane FtsW protein and peptidoglycan synthase PBP3 form a subcomplex in *Escherichia coli*. *Microbiology*, **157**, 251–259.
14. Piette, A., Fraipont, C., Den Blaauwen, T., Aarsman, M. E., Pastoret, S. & Nguyen-Disteche, M. (2004). Structural determinants required to target penicillin-binding protein 3 to the septum of *Escherichia coli*. *J. Bacteriol.* **186**, 6110–6117.
15. Nguyen-Disteche, M., Fraipont, C., Buddelmeijer, N. & Nanninga, N. (1998). The structure and function of *Escherichia coli* penicillin-binding protein 3. *Cell. Mol. Life Sci.* **54**, 309–316.
16. Georgopapadakou, N. H., Dix, B. A. & Mauriz, Y. R. (1986). Possible physiological functions of penicllin-binding proteins in *Staphylococcus aureus*. *Antimicrob. Agents Chemother.* **29**, 333–336.

17. Sung, M. T., Lai, Y. T., Huang, C. Y., Chou, L. Y., Shih, H. W., Cheng, W. C. *et al.* (2009). Crystal structure of the membrane-bound bifunctional transglycosylase PBP1b from *Escherichia coli*. *Proc. Natl Acad. Sci. USA*, **106**, 8824–8829.
18. Powell, A. J., Tomberg, J., Deacon, A. M., Nicholas, R. A. & Davies, C. (2009). Crystal structures of penicillin-binding protein 2 from penicillin-susceptible and -resistant strains of *Neisseria gonorrhoeae* reveal an unexpectedly subtle mechanism for antibiotic resistance. *J. Biol. Chem.* **284**, 1202–1212.
19. Sainsbury, S., Bird, L., Rao, V., Shepherd, S. M., Stuart, D. I., Hunter, W. N. *et al.* (2011). Crystal structures of penicillin-binding protein 3 from *Pseudomonas aeruginosa*: comparison of native and antibiotic-bound forms. *J. Mol. Biol.* **405**, 173–184.
20. Han, S., Zaniewski, R. P., Marr, E. S., Lacey, B. M., Tomaras, A. P., Evdokimov, A. *et al.* (2010). Structural basis for effectiveness of siderophore-conjugated monocarbams against clinically relevant strains of *Pseudomonas aeruginosa*. *Proc. Natl Acad. Sci. USA*, **107**, 22002–22007.
21. Contreras-Martel, C., Job, V., Di Guilmi, A. M., Vernet, T., Dideberg, O. & Dessen, A. (2006). Crystal structure of penicillin-binding protein 1a (PBP1a) reveals a mutational hotspot implicated in β-lactam resistance in *Streptococcus pneumoniae*. *J. Mol. Biol.* **355**, 684–696.
22. Pares, S., Mouz, N., Petillot, Y., Hakenbeck, R. & Dideberg, O. (1996). X-ray structure of *Streptococcus pneumoniae* PBP2x, a primary penicillin target enzyme. *Nat. Struct. Biol.* **3**, 284–289.
23. Lovering, A. L., de Castro, L. H., Lim, D. & Strynadka, N. C. (2007). Structural insight into the transglycosylation step of bacterial cell-wall biosynthesis. *Science*, **315**, 1402–1405.
24. Lim, D. & Strynadka, N. C. (2002). Structural basis for the β lactam resistance of PBP2a from methicillin-resistant *Staphylococcus aureus*. *Nat. Struct. Biol.* **9**, 870–876.
25. Adams, P. D., Afonine, P. V., Bunkoczi, G., Chen, V. B., Davis, I. W., Echols, N. *et al.* (2010). PHENIX: a comprehensive Python-based system for macromolecular structure solution. *Acta Crystallogr., Sect. D: Biol. Crystallogr.* **66**, 213–221.
26. Gouet, P., Courcelle, E., Stuart, D. I. & Metoz, F. (1999). ESPript: multiple sequence alignments in PostScript. *Bioinformatics*, **15**, 305–308.
27. Lovering, A. L., De Castro, L. & Strynadka, N. C. (2008). Identification of dynamic structural motifs involved in peptidoglycan glycosyltransfer. *J. Mol. Biol.* **383**, 167–177.
28. Goffin, C., Fraipont, C., Ayala, J., Terrak, M., Nguyen-Disteche, M. & Ghuysen, J. M. (1996). The non-penicillin-binding module of the tripartite penicillin-binding protein 3 of *Escherichia coli* is required for folding and/or stability of the penicillin-binding module and the membrane-anchoring module confers cell septation activity on the folded structure. *J. Bacteriol.* **178**, 5402–5409.
29. Punta, M., Coggill, P. C., Eberhardt, R. Y., Mistry, J., Tate, J., Boursnell, C. *et al.* (2012). The Pfam protein families database. *Nucleic Acids Res.* **40**, D290–D301.
30. Krissinel, E. & Henrick, K. (2004). Secondary-structure matching (SSM), a new tool for fast protein structure alignment in three dimensions. *Acta Crystallogr., Sect. D: Biol. Crystallogr.* **60**, 2256–2268.
31. Krissinel, E. & Henrick, K. (2007). Inference of macromolecular assemblies from crystalline state. *J. Mol. Biol.* **372**, 774–797.
32. Tame, J. R. H. (1999). Scoring functions: a view from the bench. *J. Comput.-Aided Mol. Des.* **13**, 99–108.
33. Tame, J. R. H. (2005). Scoring functions—the first 100 years. *J. Comput.-Aided Mol. Des.* **19**, 445–451.
34. Kishida, H., Unzai, S., Roper, D. I., Lloyd, A., Park, S. Y. & Tame, J. R. H. (2006). Crystal structure of penicillin binding protein 4 (dacB) from *Escherichia coli*, both in the native form and covalently linked to various antibiotics. *Biochemistry*, **45**, 783–792.
35. Georgopapadakou, N. H., Smith, S. A. & Bonner, D. P. (1982). Penicillin-binding proteins in a *Staphylococcus aureus* strain resistant to specific β-lactam antibiotics. *Antimicrob. Agents Chemother.* **22**, 172–175.
36. Contreras-Martel, C., Amoroso, A., Woon, E. C., Zervosen, A., Inglis, S., Martins, A. *et al.* (2011). Structure-guided design of cell wall biosynthesis inhibitors that overcome β-lactam resistance in *Staphylococcus aureus* (MRSA). *ACS Chem. Biol.* **6**, 943–951.
37. Tomberg, J., Unemo, M., Davies, C. & Nicholas, R. A. (2010). Molecular and structural analysis of mosaic variants of penicillin-binding protein 2 conferring decreased susceptibility to expanded-spectrum cephalosporins in *Neisseria gonorrhoeae*: role of epistatic mutations. *Biochemistry*, **49**, 8062–8070.
38. Josephine, H. R., Charlier, P., Davies, C., Nicholas, R. A. & Pratt, R. F. (2006). Reactivity of penicillin-binding proteins with peptidoglycan-mimetic β-lactams: what's wrong with these enzymes? *Biochemistry*, **45**, 15873–15883.
39. Page, M. G. P. (2012). Beta-lactam antibiotics. In *Antibiotic Discovery and Development* (Dougherty, T. J. & Pucci, M. J., eds), Springer, Berlin, Germany.
40. Clarke, T. B., Kawai, F., Park, S. Y., Tame, J. R. H., Dowson, C. G. & Roper, D. I. (2009). Mutational analysis of the substrate specificity of *Escherichia coli* penicillin binding protein 4. *Biochemistry*, **48**, 2675–2683.
41. Pratt, R. F. (2008). Substrate specificity of bacterial DD-peptidases (penicillin-binding proteins). *Cell. Mol. Life Sci.* **65**, 2138–2155.
42. Sauvage, E., Herman, R., Petrella, S., Duez, C., Bouillenne, F., Frere, J. M. & Charlier, P. (2005). Crystal structure of the *Actinomadura* R39 DD-peptidase reveals new domains in penicillin-binding proteins. *J. Biol. Chem.* **29**, 29.
43. Nicholas, R. A., Krings, S., Tomberg, J., Nicola, G. & Davies, C. (2003). Crystal structure of wild-type penicillin-binding protein 5 from *Escherichia coli*: implications for deacylation of the acyl-enzyme complex. *J. Biol. Chem.* **278**, 52826–52833.
44. Nicola, G., Tomberg, J., Pratt, R. F., Nicholas, R. A. & Davies, C. (2010). Crystal structures of covalent complexes of β-lactam antibiotics with *Escherichia coli* penicillin-binding protein 5: toward an understanding of antibiotic specificity. *Biochemistry*, **49**, 8094–8104.

45. Sauvage, E., Powell, A. J., Heilemann, J., Josephine, H. R., Charlier, P., Davies, C. & Pratt, R. F. (2008). Crystal structures of complexes of bacterial DD-peptidases with peptidoglycan-mimetic ligands: the substrate specificity puzzle. *J. Mol. Biol.* **381**, 383–393.
46. Otwinowski, Z. & Minor, W. (1997). Processing of X-ray diffraction data collected in oscillation mode. *Methods Enzymol.* **276**, 307–326.
47. Schneider, T. R. & Sheldrick, G. M. (2002). Substructure solution with SHELXD. *Acta Crystallogr., Sect. D: Biol. Crystallogr.* **58**, 1772–1779.
48. Vonrhein, C., Blanc, E., Roversi, P. & Bricogne, G. (2007). Automated structure solution with autoSHARP. *Methods Mol. Biol.* **364**, 215–230.
49. Abrahams, J.-P. & Leslie, A. G. W. (1996). Methods used in the structure determination of bovine mitochondrial F1 ATPase. *Acta Crystallogr., Sect. D: Biol. Crystallogr.* **52**, 30–42.
50. Emsley, P., Lohkamp, B., Scott, W. G. & Cowtan, K. (2010). Features and development of Coot. *Acta Crystallogr., Sect. D: Biol. Crystallogr.* **66**, 486–501.
51. Murshudov, G. N., Vagin, A. A. & Dodson, E. J. (1997). Refinement of macromolecular structures by the maximum-likelihood method. *Acta Crystallogr., Sect. D: Biol. Crystallogr.* **53**, 240–255.
52. Brown, P. H. & Schuck, P. (2008). A new adaptive grid-size algorithm for the simulation of sedimentation velocity profiles in analytical ultracentrifugation. *Comput. Phys. Commun.* **178**, 105–120.

JVI Journals ASM.org

Structural Basis for Broad Detection of Genogroup II Noroviruses by a Monoclonal Antibody That Binds to a Site Occluded in the Viral Particle

Grant S. Hansman,[a,b] David W. Taylor,[c,d] Jason S. McLellan,[b] Thomas J. Smith,[e] Ivelin Georgiev,[b] Jeremy R. H. Tame,[f] Sam-Yong Park,[f] Makoto Yamazaki,[g] Fumio Gondaira,[g] Motohiro Miki,[a,g] Kazuhiko Katayama,[a] Kazuyoshi Murata,[d] and Peter D. Kwong[b]

Department of Virology II, National Institute of Infectious Diseases, Tokyo, Japan[a]; Vaccine Research Center, National Institute of Allergy and Infectious Diseases, National Institutes of Health, Bethesda, Maryland, USA[b]; Department of Molecular Biophysics and Biochemistry, Yale University School of Medicine, New Haven, Connecticut, USA[c]; National Institute for Physiological Sciences, Okazaki, Japan[d]; Donald Danforth Plant Science Center, Saint Louis, Missouri, USA[e]; Protein Design Laboratory, Yokohama City University, Yokohama, Japan[f]; and Denka-Seiken Co. Ltd., Niigata, Japan[g]

Human noroviruses are genetically and antigenically highly divergent. Monoclonal antibodies raised in mice against one kind of norovirus virus-like particle (VLP), however, were found to have broad recognition. In this study, we present the crystal structure of the antigen-binding fragment (Fab) for one of these broadly reactive monoclonal antibodies, 5B18, in complex with the capsid-protruding domain from a genogroup II genotype 10 (GII.10) norovirus at 3.3-Å resolution and, also, the cryo-electron microscopy structure of the GII.10 VLP at ~10-Å resolution. The GII.10 VLP structure was more similar in overall architecture to the GV.1 murine norovirus virion than to the prototype GI.1 human norovirus VLP, with the GII.10 protruding domain raised ~15 Å off the shell domain and rotated ~40° relative to the GI.1 protruding domain. In the crystal structure, the 5B18 Fab bound to a highly conserved region of the protruding domain. Based on the VLP structure, this region is involved in interactions with other regions of the capsid and is buried in the virus particle. Despite the occluded nature of the recognized epitope in the VLP structure, enzyme-linked immunosorbent assay (ELISA) binding suggested that the 5B18 antibody was able to capture intact VLPs. Together, the results provide evidence that the norovirus particle is capable of extreme conformational flexibility, which may allow for antibody recognition of conserved surfaces that would otherwise be buried on intact particles.

The family *Caliciviridae* contains four genera, *Norovirus*, *Sapovirus*, *Lagovirus*, and *Vesivirus*, which include norovirus, sapovirus, rabbit hemorrhagic disease virus, and feline calicivirus strains, respectively. Human noroviruses are the dominant cause of outbreaks of gastroenteritis and are genetically and antigenically distinct (21). Two main genogroups (GI and -II) of human noroviruses are mostly responsible for causing human infections, and these two genogroups are further subdivided into numerous genotypes (GI.1 to -8 and GII.1 to -17) (72). The human norovirus genome has three open reading frames (ORF1 to -3), where ORF1 encodes the nonstructural proteins, ORF2 encodes the capsid protein, and ORF3 encodes a small structural protein. Human noroviruses cannot be grown in cell culture, but the expression of the capsid protein in a baculovirus expression system leads to the self-assembly of nucleic acid-free virus-like particles (VLPs) that are believed to be morphologically and antigenically similar to the native virion (27).

The cryo-electron microscopy (cryo-EM) and X-ray crystal structures of the prototype norovirus VLP (GI.1, Norwalk virus) show that the VLP form a T=3 icosahedral structure (53, 54). The VLP can be divided into two domains, the shell (S) and the protruding (P) domains. The S domain forms a scaffold surrounding the RNA, whereas the P domain, which is further subdivided into P1 and P2 subdomains, is thought to contain the determinants of cell attachment and strain diversity (27, 53, 60). The P domain forms 90 dimer subunits, termed A/B and C/C. Interestingly, the P domains alone can be expressed in *Escherichia coli*, and these form P domain dimers that are biologically relevant (60). The X-ray crystal structures of several human norovirus P domains (GI.1, GII.4, GII.10, and GII.12) indicate that their overall structures are similar and resemble the P domain on the VLPs, with a single α-helix in the P1 subdomain and six antiparallel β-strands in the P2 subdomain (7, 10, 13, 22). The X-ray crystal structure of a GV.1 murine norovirus P domain reveals a structure that is similar overall to the human norovirus P domains (63). However, cryo-electron microscopy (cryo-EM) studies show that in the GV.1 murine norovirus virion, the P domain is raised off the S domain by ~16 Å (30), while in the GI.1 and GII.4 (Grimsby virus strain) human norovirus VLPs, the P domain rests directly on the S domain (12, 53, 54). In addition, the GV.1 murine norovirus P domain is rotated 40° clockwise with respect to the GI.1 and GII.4 human norovirus P domains.

Human noroviruses are generally detected using reverse transcription-PCR (RT-PCR) with degenerate primers or enzyme-linked immunosorbent assay (ELISA) with norovirus-specific antibodies. Many of the polyclonal and monoclonal antibodies (MAbs) used in the ELISA kits were developed in mice immunized with norovirus VLPs (15, 28, 55, 57), and most have broad recognition (21, 39, 40, 50, 59, 70). Several antibodies are found to bind to the S domain (39, 70), while others bound to the P domain (50, 59). However,

Received 23 November 2011 Accepted 10 January 2012
Published ahead of print 25 January 2012
Address correspondence to Peter D. Kwong, pdkwong@nih.gov, or Kazuyoshi Murata, kazum@nips.ac.jp.
Supplemental material for this article may be found at http://jvi.asm.org/.

doi:10.1128/JVI.06868-11

structural details of the antibody mode of binding to the VLPs, S domain or P domain, have been lacking. In the studies presented here, we used X-ray crystallography to define the recognition site of the broadly reactive antibody 5B18 on the norovirus GII.10 P domain, cryo-EM to determine the structure of the intact GII.10 VLP, and ELISA to determine whether this antibody recognizes intact or disassembled virus particles. Overall, the findings have implications related to the dynamic nature of the P domain in the context of the norovirus VLP and to its recognition by antibody.

MATERIALS AND METHODS

Norovirus VLP expression. The GII.4 Saga (GenBank accession number BAG70515), GII.10 Vietnam026 (GenBank accession number AF504671) (23), and GII.12 Hiro (GenBank accession number AB044366) (23) VLPs were expressed as previously described (23). The VLPs were purified using CsCl equilibrium gradient ultracentrifugation at 35,000 rpm for 24 h at 4°C (Beckman SW55 rotor). A distinct viral band was removed from the side of the tube with a syringe and the VLPs were stored in phosphate-buffered saline (PBS) (pH 7.3) at 4°C. The integrity of the VLPs was confirmed by negative-stain EM. Briefly, the VLP samples were applied to a carbon-coated 300-mesh EM grid and stained with 2% uranyl acetate (pH 4). Grids were examined using a Jeol JEM-1220 transmission electron microscope operated at 80 kV.

Antibody ELISA binding to GII.4, GII.10, and GII.12 VLPs. An antibody ELISA was used to compare the cross-reactivities of VLPs from the three different GII norovirus genotypes (GII.4, GII.10, and GII.12) with 5B18 IgG. Wells of 96-well microtiter plates (MaxiSorp; Nunc, Denmark) were each coated with 100 μl of ~100 ng of purified VLPs (in PBS, pH 7.3) and incubated overnight at 4°C. The wells were washed four times with PBS containing 0.1% (vol/vol) Tween 20 (PBS-T) and then were blocked with PBS containing 5% (wt/vol) skim milk for 1 h at room temperature. After the wells were washed four times with PBS-T, 100 μl of 2-fold serially diluted horseradish peroxidase (HRP)-conjugated labeled 5B18 IgG, from a 1:5,000 starting dilution in PBS containing 0.05% (wt/vol) skim milk, was added to each well, and the plates were incubated for 1 h at 37°C. The wells were washed four times with PBS-T, and then 100 μl of 3,3′,5,5′-tetramethylbenzidine substrate was added to each well. The reaction was stopped by the addition of 100 μl of 2 N H_2SO_4 to each well, and the absorbance was measured at 450 nm (A_{450}). The titer was expressed as the reciprocal of the highest dilution of antiserum giving a value of A_{450} of >0.2, as previously described (21).

Western blotting. The VLPs and P domains were separated by SDS-PAGE and electrotransferred to polyvinylidene difluoride (PVDF) membranes by using iBLOT, following the manufacturer's protocol. Proteins were detected with 5B18 IgG at a dilution of 1:5,000, and then, following the manufacturer's instructions, the blots were developed by chemiluminescence using enhanced chemiluminescence (ECL) detection reagent (Amersham Biosciences, England).

Protein expression and purification of GII.10 P domain. The GII.10 P domain was expressed in *E. coli* and purified as previously described (22). Briefly, the P domain was optimized for *E. coli* expression, cloned in a modified pMal-c2x vector at the BamHI and NotI restriction sites (New England BioLabs), and transformed into BL21(DE3) cells (Invitrogen). Expression was induced with IPTG (isopropyl-β-D-thiogalactopyranoside) (1 mM) for 18 h at 22°C. After a series of purification steps and protease cleavage, the P domain was concentrated to 2 to 10 mg/ml and stored in gel filtration buffer (0.35 M NaCl, 2.5 mM Tris, pH 7.0, 0.02% NaN_3).

Preparation of 5B18 Fab fragment. The 5B18 IgG monoclonal antibody was produced from a mouse immunized with GII.4 norovirus-445 VLPs (GenBank accession number DQ093064) (Denkaseiken, Japan). The 5B18 IgG is currently used as a GII broad-range capture antibody in a commercially available ELISA kit (Denkaseiken, Japan). The 5B18 Fab was prepared using a modified method (34). Approximately 60 mg of purified 5B18 IgG was used for Fab preparation. IgG was reduced in 100 mM dithiothreitol (DTT) (pH 7.6) for 1 h at 37°C. The reduced IgG was added to a dialysis cassette, and the DTT was removed by placing the cassette in GFB (0.35 M NaCl, 2.5 mM Tris, pH 7.0, 0.02% NaN_3) supplemented with 20 mM HEPES (pH 7.7) for 1 h at 4°C. The IgG was alkylated in the same buffer supplemented with 2 mM iodoacetamide for 48 h at 4°C, and then the cassette was transferred to a fresh solution without the iodoacetamide for 1 h at 4°C. The IgG was concentrated to 5 mg/ml and then digested with papain using a commercial kit (Pierce, Rockford, United States). The Fab was separated from the Fc in a protein A column, and the resulting Fab was further purified by size exclusion chromatography with a Superdex 200 column (GE), concentrated to 5 mg/ml, and stored in GFB. The purified GII.10 P domain and Fab were mixed 1.4:1 for 1 h at 25°C, and finally, the GII.10 P domain-Fab complex was purified by size exclusion chromatography.

Preparation and cocrystallization of GII.10 P domain-Fab complex for X-ray crystallography. Crystals of the GII.10 P domain-Fab complex were grown by the hanging drop vapor diffusion method, mixing the protein and reservoir solution (40% [vol/vol] polyethylene glycol [PEG] 400, 5% [wt/vol] PEG 3350, and 0.1 M acetic acid, pH 5.5) (42) in a 1:1 ratio. Crystals grew over 1 week at a temperature of 20°C. Prior to data collection, crystals were transferred to 50% (vol/vol) PEG 400.

X-ray crystallography data collection, structure solution, and refinement. X-ray diffraction data were collected at the Southeast Regional Collaborative Access Team (SER-CAT) beamline 22-BM at the Advanced Photon Source, Argonne National Laboratory, Argonne, IL, and processed with HKL2000 (49). Despite the large size of the crystals (perfectly formed pyramids of up to 0.3 mm per edge), the diffraction data were poor due to split reflections, high background, and most diffraction extending to less than 4 Å. These resulted in Chi^2 values of 0 for several wedges of data. Despite these difficulties, relatively complete data (90%) was obtained from 180 degrees of oscillation, though with lower than expected redundancy (2.7-fold), and the overall quality of data which passed the Chi^2 tests appeared fine. Structures were solved by molecular replacement in PHASER (44), using the structure with Protein Data Bank identifier (PDB ID) 3ONU for the GII.10 P domain and the structure with PDB ID 1WEJ for the Fab as a search model. Manual model building was performed in COOT (18), and positional refinement together with translation/liberation/screw (TLS) refinement were performed using REFMAC (14) and PHENIX (1).

Cryo-EM data collection and refinement. VLPs at a concentration of 1.0 mg/ml were applied to a glow-discharged Quantifoil R1.2/1.3 Mo 200-mesh holey carbon grid with a thin layer of carbon over the holes. The sample was rapidly plunged into liquid ethane after automatic blotting for 7 to 8 s at 8°C and 100% humidity using an FEI MarkIV Vitrobot. Grids were examined with a JEOL JEM-2200FFC microscope equipped with a field emission gun and an in-column (omega-type) energy filter operated at an acceleration voltage of 200 kV. Images of the frozen VLPs were collected at a nominal magnification of 40,000 using a 4k × 4k (4,096- by 4,096-pixel) Tietz charge-coupled-device (CCD) camera, resulting in a pixel size of 2.4 Å. Particles were extracted from raw micrographs using the swarm semiautomatic particle-picking algorithm in EMAN2 into boxes of 250 by 250 square pixels (61). The raw particles were normalized, phase flipped, and high-pass filtered before single-particle analysis. Approximately 8,000 particle images were subjected to two-dimensional (2-D) reference-free alignment and classification through several rounds of multireference alignment and multivariate statistical analysis in IMAGIC to a total of 50 classes (65). Approximately 80% of the data were used for the reconstruction. Particles with cross-correlation values 1.5 σ below the mean were not used (~20%). Representative class averages were used as the basis for initial model generation in EMAN2. The initial model with the best match between reprojections and class averages was chosen as the starting model for several rounds of projection-matching refinement with increasing angular sampling. The final reconstruction, at ~10-Å resolution (0.5 Fourier shell correlation [FSC] criterion), was used for atomic coordinate fitting and structure comparison in Chimera (version 1.5.3) (52).

Structure analysis, sequence analysis, and figures. Figures were rendered using PyMOL (version 1.2r3; Schroedinger LLC) and Chimera (version 1.5.3) (52). The N-terminal amino acid sequences for the Fab heavy and kappa (κ) chains were determined at the Columbia University Medical Center, Protein Core Facility. Degenerate primers for the Fab sequence were designed from constant regions and from the N-terminal amino acid sequence based on closely matching murine antibody N-terminal nucleotide sequences in GenBank. Norovirus complete-capsid amino acid sequences were aligned and analyzed with GenetyxMac software (version 16.0.0).

Antibody ELISA binding to GII.10 VLPs at different pHs. An antibody ELISA was used to determine the ability of 5B18 IgG to bind to GII.10 VLPs. The GII.10 VLPs were diluted in PBS at pHs 5.3, 6.3, 7.3, 8.3, and 9.3 to a final concentration of 7.5 μg/ml. At high PBS pHs, the VLPs were found to be partially broken, while at low pHs, most of the VLPs were intact. Wells of 96-well microtiter plates (MaxiSorp; Nunc, Denmark) were each coated with 100 μl of 7.5 μg/ml of VLPs at the different pHs and incubated overnight at 4°C. The VLPs were detected as described above, except that 5B18 IgG and goat HRP–anti-mouse IgG (used as a secondary antibody) replaced the HRP-labeled 5B18 IgG. After the addition of the secondary antibody, the wells were washed four times with PBS-T, and then 100 μl of substrate *o*-phenylenediamine and H_2O_2 was added to each well and the plates left in the dark for 30 min at room temperature. The reaction was stopped by the addition of 50 μl of 2 N H_2SO_4 to each well, and the absorbance was measured at 492 nm (A_{492}).

Sequence conservation on the VLP and P domain. To show the sequence conservation on the GII VLP, a model of the GII.10 VLP was built as described previously (22) using the unbound GII.10 P domain structure (PDB ID 3ONU) and the S domain from the Norwalk virus capsid structure (PDB ID 1IHM). Amino acid sequence conservation was analyzed as previously described (22). Briefly, an alignment of a representative set of GII sequences was used to compute residue conservation scores using the AL2CO server (51) and mapped (using a color range for highly variable to highly conserved residues) onto the surface of the GII.10 VLP model and unbound GII.10 P domain structure.

Accession numbers. Atomic coordinate and structure factors of the X-ray crystal structure were deposited in the Protein Data Bank under accession number 3V7A. The 3-D cryo-EM map was deposited in the EMDataBank with accession number EMD-5374.

RESULTS

5B18 binds to several GII genotypes. To confirm the ability of the 5B18 IgG to bind diverse GII norovirus genotypes, we expressed VLPs from three GII genotypes (GII.4, GII.10, and GII.12) and examined the binding using ELISA and Western blotting. The EM results showed that GII.4 VLPs were a mixture of small and native-size particles, while the GII.10 and GII.12 VLPs were mostly of native size (data not shown). The ELISA results showed that 5B18 IgG was capable of cross-reacting with all three GII genotypes having an equal titer of 320,000 (see Fig. S1A in the supplemental material). The Western blotting results also showed that the 5B18 IgG could detect the three GII genotypes (see Fig. S1B).

X-ray crystal structure of GII.10 P domain-Fab complex. The GII.10 P domain was used to determine the precise binding location of the 5B18 antibody on the norovirus capsid using X-ray crystallography. The GII.10 P domain and Fab proteins were mixed together (1.4:1 molar ratio) for 1 h at room temperature. The GII.10 P domain-Fab complex was purified using size exclusion chromatography. Two main peaks were observed, corresponding to the complex and free P domain (data not shown). The fractions containing the GII.10 P domain-Fab complex were pooled and concentrated to ~4 mg/ml, and the complex was crystallized by the hanging-drop vapor diffusion method. A single GII.10 P domain-Fab complex crystal diffracted X rays to ~3.3 Å. The structure was solved using molecular replacement with a GII.10 P domain monomer (PDB ID 3ONU) and a mouse Fab (PDB ID 1WEJ) as search models. Molecular replacement indicated that two P domain monomers and two 5B18 Fabs each containing a kappa (κ) chain and heavy chain were in the asymmetrical unit and these were related by a noncrystallographic 2-fold. Water molecules were not added to the structure since the resolution was at 3.3 Å. The 5B18 Fab was shown to bind to the wall of the P1 subdomain and involved a monomeric interaction with the P1 subdomain (Fig. 1A). The electron densities of the P domains and 5B18 Fabs were generally well defined, and refinement led to an R_{value} of 0.230 (R_{free} of 0.283) (Table 1; also see Fig. S2 in the supplemental material). The P domain dimer had a single helix in each P1 subdomain and six antiparallel β-strands in each P2 subdomain as previously described (22).

GII.10 P domain interaction with the 5B18 Fab. The total interface area of the GII.10 P domain and 5B18 Fab was 1,500 Å^2 (770 Å^2 on the P domain and 730 Å^2 on the 5B18 Fab), as calculated using PISA software (33). The GII.10 P domain and 5B18 Fab interaction included nine hydrogen bonds, eight of which were formed between the P1 subdomain and κ chain and one between the P1 subdomain and heavy chain (Fig. 1B; also see Table S1 in the supplemental material). Six P1 subdomain amino acids interacted with the 5B18 Fab, Tyr533 formed a single hydrogen bond with Tyr92κ, Thr534 formed three hydrogen bonds with Gly93κ and one hydrogen bond with Trp97κ, Leu535 formed a hydrogen bond with Tyr32κ, Glu496 formed a hydrogen bond with Tyr92κ, Asn530 formed a hydrogen bond with Ser94κ, and Val433 formed a hydrogen bond with Asn52 heavy chain. Superposition of the apo GII.10 P domain dimer and the Fab-bound GII.10 P domain showed that each of the P1 subdomains shifted slightly (~1 to 2 Å) toward the center of the dimer, while the P2 subdomain showed little conformational change (see Fig. S3 in the supplemental material). The electrostatic potential of the Fab was calculated (16), and the interacting residues on the P domain bound at two negatively charged pockets on the Fab at the variable regions (Fig. 2).

Conservation of the 5B18 Fab-binding site on GII P domains. The 5B18 Fab formed hydrogen bonds with residues at three different sites on the P1 subdomain, termed A, B, and C (Fig. 3). An amino acid alignment of representatives from 10 GII norovirus genotypes indicated that Val433 (site A) was the most variable, with other genotypes having threonine, serine, asparagine, leucine, or methionine at this position. Thr534 (site C) was mostly conserved, as the only other amino acid at this position was a serine. Glu496 (site B), Asn530 (site C), Tyr533 (site C), and Leu535 (site C) were all highly conserved among the representative GII genotypes. Superposition of other known GII norovirus P domains (GV.1, GII.4-TCH05, GII.4-VA387, GII.12, GII.9-VA207, and GI.1) showed that the equivalent GII.10 interacting side chains were mostly in the same conformation (see Fig. S4 in the supplemental material). GI norovirus side chains also appeared to be similar to the GII.10 interacting side chains (see Fig. S4).

GII.10 VLP cryo-EM structure. From the general location of the epitope (Fig. 1) and the known structures of other caliciviruses (7, 10, 13, 22), it was not clear how the monoclonal antibody, raised against intact VLPs, could bind at this occluded site on intact particles. To this end, the cryo-EM structure of the GII.10 VLP (in an unbound state) was determined to define the arrange-

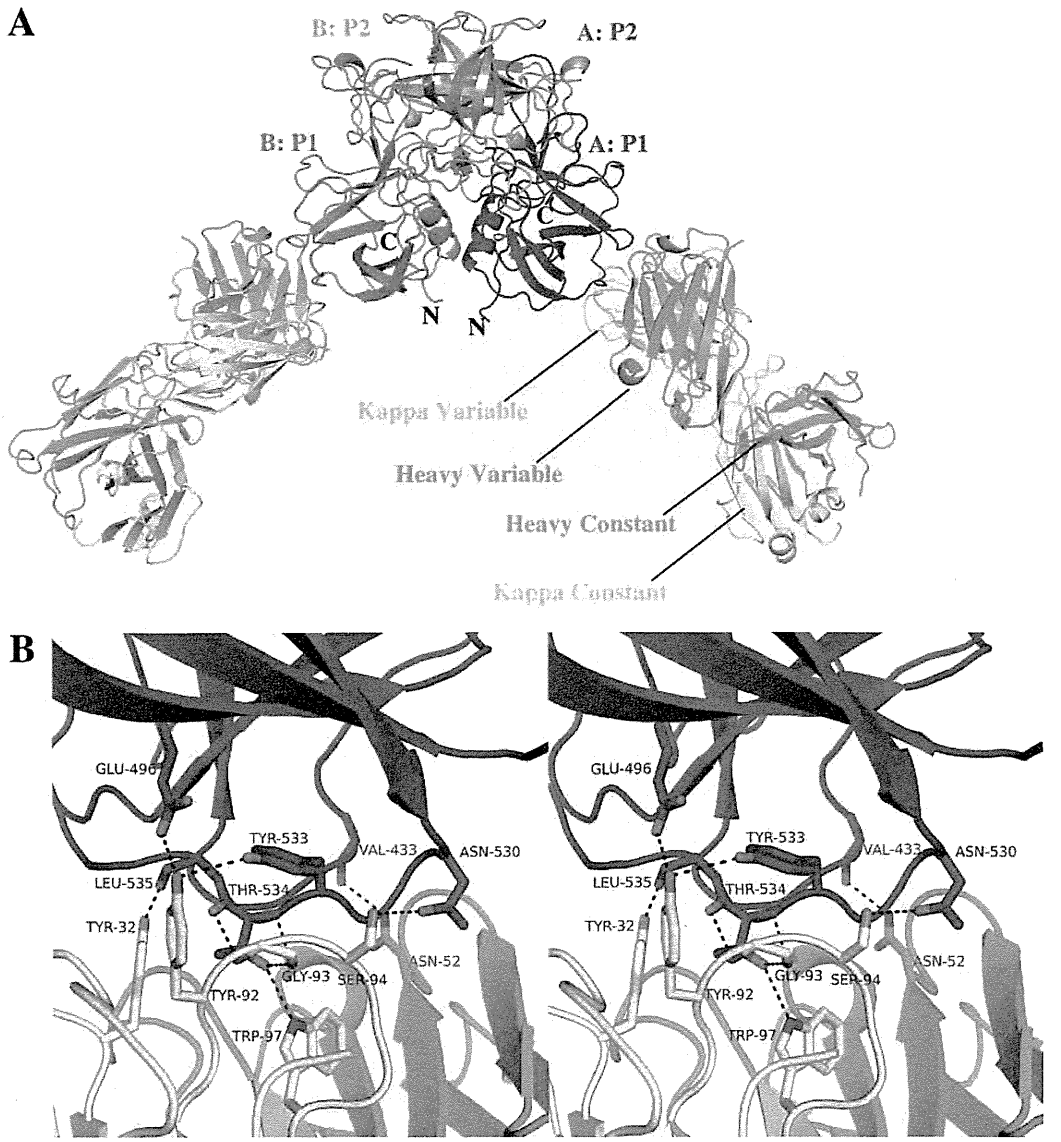

FIG 1 The X-ray crystal structure of the GII.10 P domain-Fab complex shows that the Fab bound to the lower side of the P1 subdomain. The GII.10 P domain dimer is colored according to monomers and subdomains, i.e., chain A: P1 (blue), chain A: P2 (light blue), chain B: P1 (violet), and chain B: P2 (salmon), whereas the Fab is colored according to chain, i.e., κ chain (yellow) and heavy chain (green). (A) The Fab bound to the wall of the P1 subdomain (considered to be inside the virus particle) and involved a monomeric interaction. (B) A close-up stereoview of the interacting P domain residues for chain A (Val433, Glu496, Asn530, Tyr533, Thr534, and Leu535) and Fab residues (κ chain, Tyr32, Tyr92, Gly93, Ser94, and Trp97, and heavy chain, Asn52). The hydrogen bond interactions included both side chain and main chain interactions (also see Table S1 in the supplemental material).

ment of the GII.10 P domains with respect to the entire capsid. The GII.10 VLPs appeared as homogeneous, monodisperse particles in ice (see Fig. S5A in the supplemental material). Reference-free class averages of the VLPs showed icosahedral particles with spike-like structures extending from the vertices (see Fig. S5). The cryo-EM reconstruction of the GII.10 VLP at ~10-Å resolution (0.5 FSC criterion) showed several striking features (Fig. 4). The GII.10 S domain was noticeably surface exposed at the 3- and 5-fold axes (Fig. 4A). The GII.10 P domain appeared as a second outer shell, and a central section through the VLP revealed that the P domain was raised off the S domain by ~15 Å (Fig. 4B). The electron density at the tip of the P domain (the P2 subdomain) was significantly weaker than at the base of the P1 domain, suggesting that there was marked flexibility in the P2 subdomains. This was consistent with what has been observed with several other reconstructions of calicivirus particles (4, 5) and suggests that there is a great deal of conformational heterogeneity in the P domains.

Fitting of the GII.10 P domain and P domain-Fab complex into the GII.10 VLP cryo-EM structure. At ~10-Å resolution, the GII.10 P domain monomers on the VLP were easily distinguished.

TABLE 1 Data collection and refinement statistics for the GII.10 norovirus P domain-Fab complex structure

Parameter	Value[a]
Data collection	
Space group	P 4_322
Cell dimensions	
a, *b*, *c* (Å)	145.48, 145.48, 216.33
α, β, γ (°)	90, 90, 90
Resolution (Å)	50-3.30 (3.42-3.30)[b]
R_{sym}	15.0 (55.1)
$I/\sigma I$	8.3 (1.8)
Completeness (%)	87.6 (89.0)
Redundancy	2.7 (2.7)
No. of unique reflections	31,300
Refinement	
Resolution (Å)	31.54–3.30
No. of reflections	30,833
R_{work}/R_{free}	0.227/0.283
No. of atoms	11,459
Average *B* factors (Å^2)	
Overall	84.7
P domain	82.4
Fab	86.3
Ramachandran (%)	
Outliers	0.00
Favored	93.31
RMS deviations	
Bond lengths (Å)	0.004
Bond angles (°)	0.795

[a] The data set was collected from a single crystal of the 026_P domain-Fab complex (PDB ID 3V7A).
[b] Values in parentheses are for the highest-resolution shell.

Fitting of the crystal structures of the GII.10 P domain and P domain-Fab complex into the GII.10 VLP cryo-EM map was performed manually and guided by previous fitting results of GV.1 P domain dimers into the GV.1 cryo-EM map (63). This approximate alignment was adjusted computationally using the Fit-in-Map function in UCSF Chimera (52) to a cross-correlation coefficient of 0.94 (Fig. 4). Using this method, the X-ray structure of the GII.10 P domain dimer (PDB ID 3ONU) was unambiguously fitted into the corresponding density in the cryo-EM map, except for several loops on the P2 subdomain (Fig. 4C). This is probably due to flexibility in these domains, as the electron density of the P2 subdomain loops was weak and the tips of the P2 domains were less ordered than the S domain and P1 domains in the cryo-EM reconstruction (data not shown). The P domain dimers appeared to be connected to adjacent, icosahedrally related P1 subdomains in the VLP, whereas the P2 subdomains had no such connections (Fig. 4C). When the P domain from the X-ray structure of the P domain-Fab complex was fitted into the A/B dimer subunit of the reconstruction, the 5B18 Fab was located under the neighboring P domain dimer and rested on top of the S domain at the space at the 2-fold axes (Fig. 5A). When the P domain from the X-ray structure of the P domain-Fab complex was instead fitted into the C/C dimer subunit, the 5B18 Fab made contact with a neighboring P domain dimer and clashed with a star-like protrusion on the S domain at the space at the 5-fold axes (Fig. 5B). Essentially, the epitope of 5B18 overlapped the region of the P1 subdomain that made interactions with icosahedrally related, adjacent P domains in the VLPs when in this "floating P domain" conformation. Based on this modeling, it appeared that the VLP probably could not be saturated with 5B18 antibodies, as this would create a highly unstable structure, as well as additional IgG-IgG steric clashes at the axis spaces. Two possibilities are likely, (i) that 5B18 recognition of intact norovirus particles occurs at select, transiently exposed P domains or (ii) that 5B18 recognition occurs at places where the particle has a defect, where the P domain is exposed because the particle is not appropriately formed.

The 5B18 IgG bound equally well with intact and partially broken GII.10 VLPs. To test whether 5B18 recognition occurs with intact or with broken particles, we assessed the pH behavior of 5B18 recognition, as norovirus VLPs become less stable and appear broken at high pH values (2). We observed that at low and neutral pHs (5.3, 6.3, and 7.3), the GII.10 VLPs were mostly homogenous in size and unbroken, whereas at higher pHs (8.3 and 9.3), the GII.10 VLPs appeared less homogenous in size and partially broken (Fig. 6A). The 5B18 IgG detected GII.10 VLPs at different pH values with nearly identical efficacy, regardless of the fraction of damaged particles (Fig. 6B). At pH 5.3, 6.3, and 8.3, the titer was 512,000, at pH 9.3, the titer was 1,024,000, and at pH 7.3, the titer was 2,048,000 (optical density [OD] cutoff of >0.2) (21).

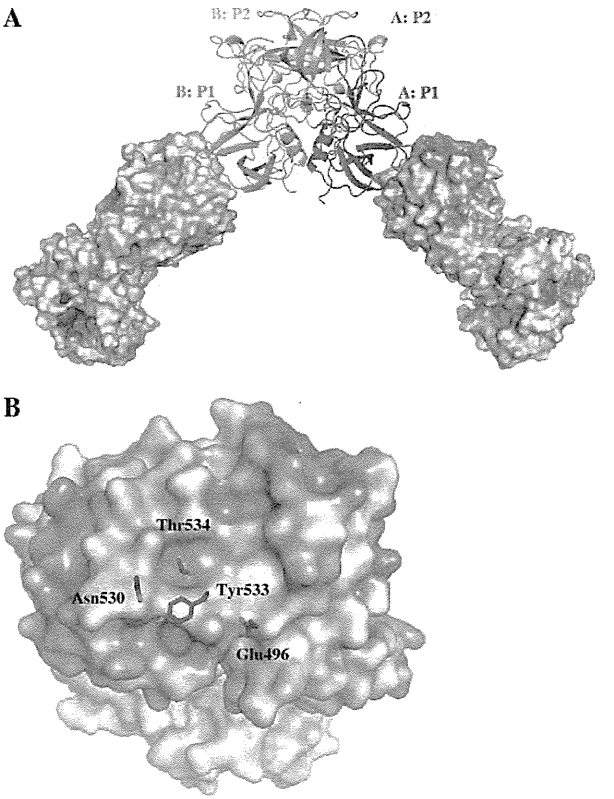

FIG 2 The binding site on the Fab was coordinated by negative charge regions on the Fab. (A) The GII.10 P domain is colored as in Fig. 1. The 5B18 Fab surface is color-coded according to electrostatic potential from red (negative charge) to blue (positive charge). (B) A close-up view of the electrostatic potential on the Fab, showing the four P domain side chain residues on chain A that interacted with the Fab. The P domain side chains bound near the negative charge (red) regions on the Fab.

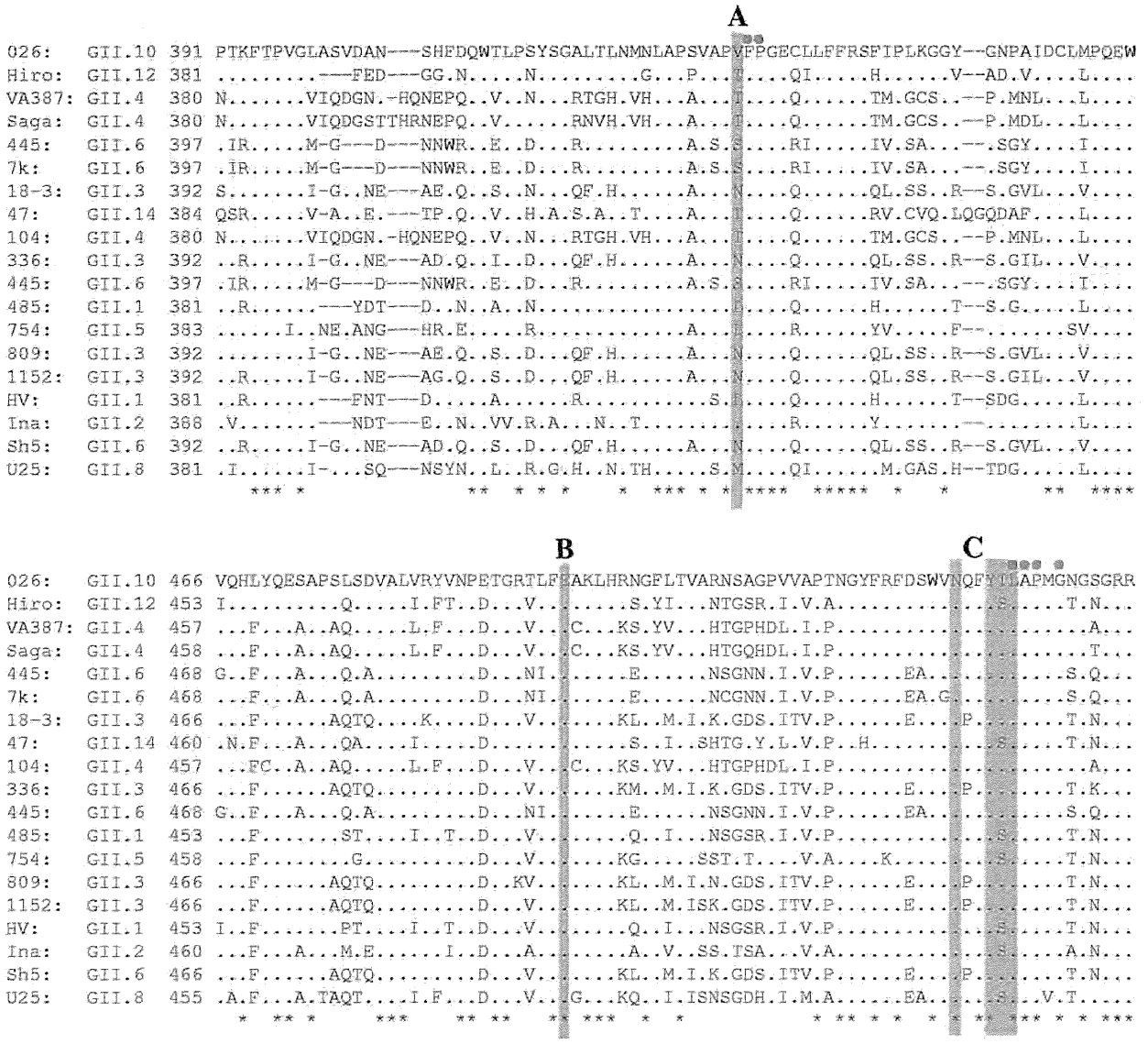

FIG 3 Amino acid alignment of GII capsid sequences indicated that four GII.10 P domain residues involved in binding 5B18 Fab were highly conserved among other GII genotypes. Ten different GII genotypes' capsid sequences were aligned (strain name is followed by genotype), and the GII.10 capsid sequence was used as the consensus (21). The GII.10 P domain residues that interacted with the 5B18 Fab involved three different sites on the P domain, termed A, B, and C. The blue shading shows the six GII.10 P domain residues that interacted with the 5B18 Fab, and from the alignment, four of six residues were highly conserved among other GII genotypes. The red circles show the suspected binding site of MAb14-1 monoclonal antibody (59).

Together, these results suggest that 5B18 appears capable of detecting nominally intact GII.10 VLPs.

Norovirus variability and 5B18 detection. As stated previously, norovirus displays considerable genetic variation. Mapping this variation onto the VLP structure shows that this variation is concentrated on the outer surface of the virion, with buried portions of the P and S domains being much more conserved (Fig. 7). If one were only able to access the outer surface of the VLP, this genetic variation would make pan-recognition extremely difficult. The 5B18 mode of recognition thus provides a mechanism to achieve broad VLP detection by recognizing a conserved surface that is transiently exposed in a dynamic manner. Indeed, the Fab footprint was highly conserved on the GII P domains (Fig. 7C).

DISCUSSION

Human noroviruses are genetically and antigenically distinct, but broad-range monoclonal antibodies capable of detecting multiple norovirus genogroups and genotypes have been described (21, 39, 40, 50, 59, 70). One such antibody, 5B18, is currently in use in a commercial norovirus ELISA detection kit (Denka Seiken, Japan) and was found to bind to numerous GII genotypes but not GI noroviruses (unpublished data). To describe the precise binding

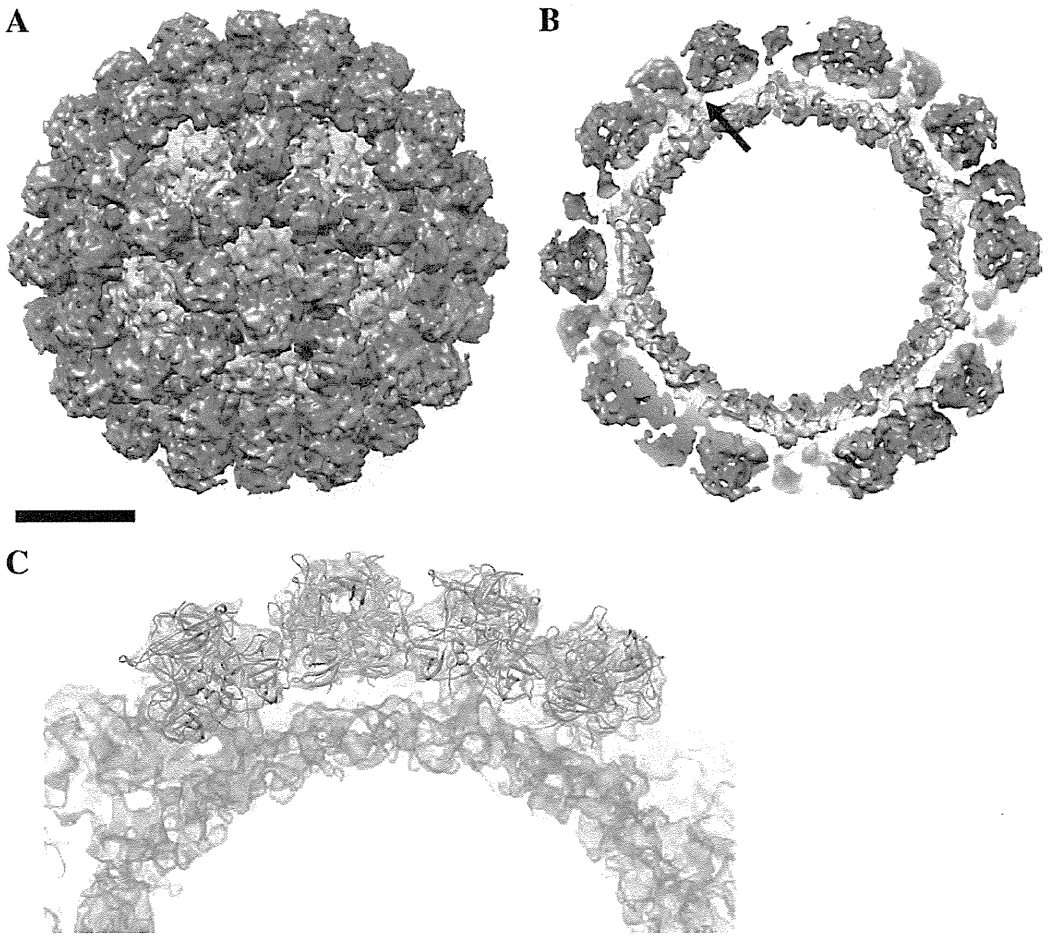

FIG 4 The cryo-EM structure of the GII.10 VLP consisted of an S domain surrounded by 90 P domain dimers. (A) The GII.10 S domain was surface exposed (yellow and yellow to green). The P domain dimers (green to blue and purple) were raised off the S domain by ~15 Å. (B) The inner surface of the S domain is colored red. The S domain was connected to the P domain monomer by a narrow hinge region (single arrow; the other hinges were not labeled for clarity). The scale bar for panels A and B indicates 100 Å. (C) Fitting and modeling of the GII.10 P domain (apo P domain structure) into the A/B dimer subunit (light blue and pink, respectively) and C/C dimer subunit (cyan).

location of 5B18, we determined the X-ray crystal structure of the GII.10 P domain-Fab complex. We also determined the cryo-EM structure of the GII.10 VLPs in an attempt to understand the 5B18 Fab binding interaction in the context of the entire virus particle.

The 5B18 Fab binds to a face of the GII.10 P1 subdomain close to the S domain and not openly exposed at the VLP surface. Six amino acid residues on the P1 subdomain make main chain and side chain interactions with the Fab. Four of these residues are highly conserved among numerous GII norovirus genotypes (Fig. 3). Variation at these residues appears to be tolerated, as the 5B18 antibody detects both GII.4 VLPs, which had Thr433 (instead of Val433), and GII.12 VLPs, which had Thr433 and Ser534 (instead of Val433 and Thr534, respectively). Surprisingly, the 5B18 Fab contact residues are almost identical to those of another broad-range monoclonal antibody, MAb14-1 (Fig. 3) (59). Furthermore, the epitopes of two other broad-range monoclonal antibodies, NV3901 and NV3912, are in this general region (50). The MAb14-1 antibody was shown to bind VLPs from many GII genotypes and several GI genotypes, including a GI.1 genotype, whereas the NV3901 and NV3912 antibodies were found to only bind GI genotypes. Interestingly, the 5B18, MAb14-1, and NV3901/NV3912 antibodies were raised in different mice immunized with different VLPs and their binding sites were all in close proximity on the P1 subdomain (50). Although the precise structural binding details of MAb14-1, NV3901, and NV3912 antibodies have not been described, it suggests that the P1 subdomain was an important antigenic site for GI and GII noroviruses. Moreover, the P1 subdomain likely contained GI and GII cross-reactive epitopes. Superpositioning of published X-ray crystal structures of norovirus P domain (GI.1, GII.4, GII.9, GII.12, and GV.1) onto the GII.10 P domain-Fab complex structure showed that three of six amino acids involved in the 5B18 Fab binding were highly conserved for three norovirus genogroups and that the conformation of their side chains closely resembles those of GII.10 (see Table S2 and Fig. S4 in the supplemental material). Taken together, the results indicate that the 5B18 binding epitope represents an important site for antibody recognition (Fig. 7).

Initially, the X-ray crystal structure of the GI.1 VLP (53) was

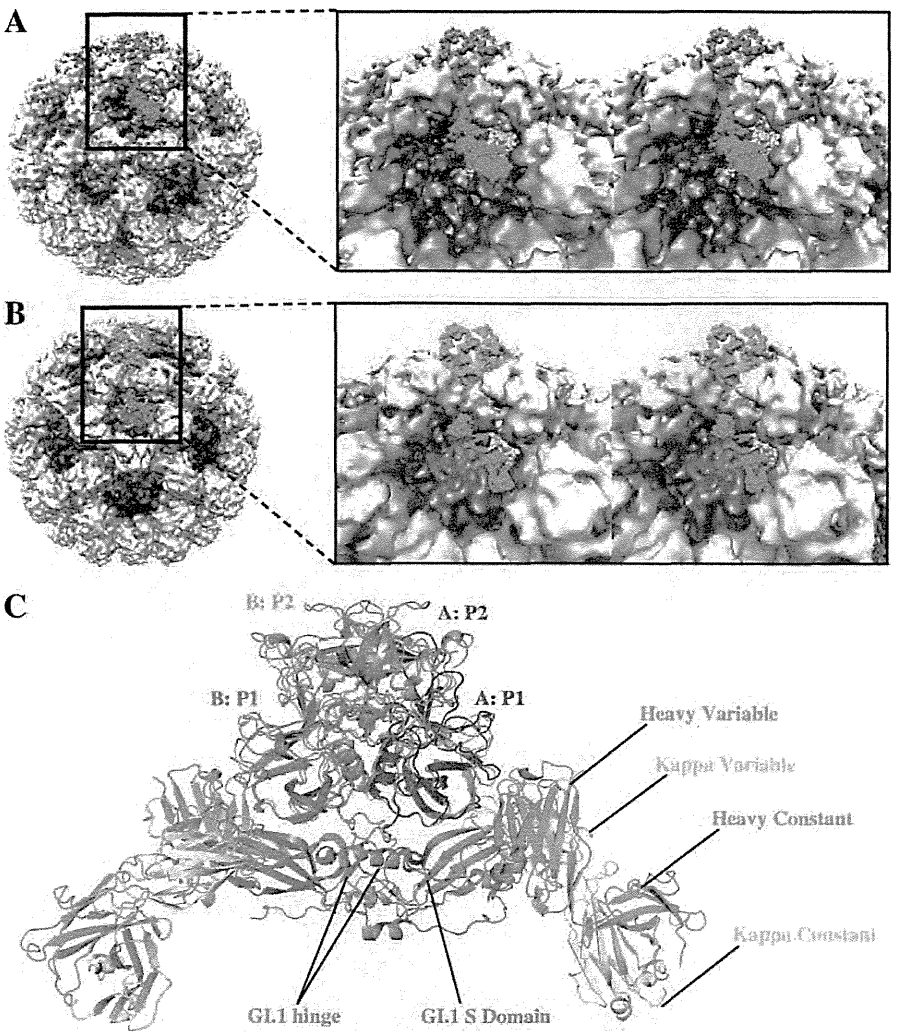

FIG 5 The X-ray crystal structure of the GII.10 P domain-Fab complex fitted into the cryo-EM structure of the GII.10 VLP and the X-ray crystal structure of the GI.1 VLP (PDB ID 1IHM). (A) The P domain (light blue and pink) from the P domain-Fab was fitted into the A/B dimer subunit on the VLP. The boxed region shows a close-up stereoview of the interaction. The Fab appeared to make slight contact with the S domain at the space at the 6-fold axes and was under a neighboring domain. (B) The P domain (cyan) from the P domain-Fab was fitted into the C/C dimer subunit on the VLP. The boxed region shows a close-up stereoview of the interaction. The Fab appeared to make contact with a raised S domain structure at the space at the 5-fold axes and was for the most part hidden under a neighboring domain. (C) The GII.10 P domain (colored as in Fig. 1 and rotated 90° from the views in Fig. 5A and 5B) was highly similar to the GI.1 P domain (light gray), but the Fabs clashed with the GI.1 S domain (orange).

used for fitting the GII.10 P domain-Fab complex and to describe the binding interaction in the context of the entire particle. The P domains of GI.1 and GII.10 matched well (root mean square deviation [RMSD], 1.3 Å), but the 5B18 Fab clashed with the GI.1 S domain (Fig. 5C). Indeed, the P domains in GI.1 VLPs rest on the S domains, and this necessarily placed most of the Fab structure into a position that overlapped the S domain (Fig. 5C). In an attempt to understand the 5B18 antibody interaction in the context of a GII VLP, the cryo-EM structure of the GII.10 VLP was determined to an ~10-Å resolution. Recent cryo-EM studies have shown that GI.1 and GV.1 norovirus capsid structures are strikingly different (30, 67), whereas another study indicated that GI.1 and GII.4 (Grimsby virus) capsids are highly similar (12). The cryo-EM structure of the GII.10 VLPs showed several structural similarities to the GV.1 virion, including a raised P domain, P1-P1 subdomain contacts, and an extended hinge region (see Fig. S6 in the supplemental material). In addition, the GII.10 and GV.1 P domain dimers were rotated ~40° clockwise compared to the orientation of the GI.1 P domain dimer (data not shown). Fitting of the X-ray crystal structure of the GII.10 P domain-Fab complex into the GII.10 VLP structure showed that the P domain could be positioned unambiguously into the P domain density of the EM map; however, this placement resulted in significant overlap between Fab and neighboring P and S domains in the virus particle (Fig. 5). One potential explanation for this result is that the VLPs flexibly expose the P domain to the 5B18 antibody by rotating the

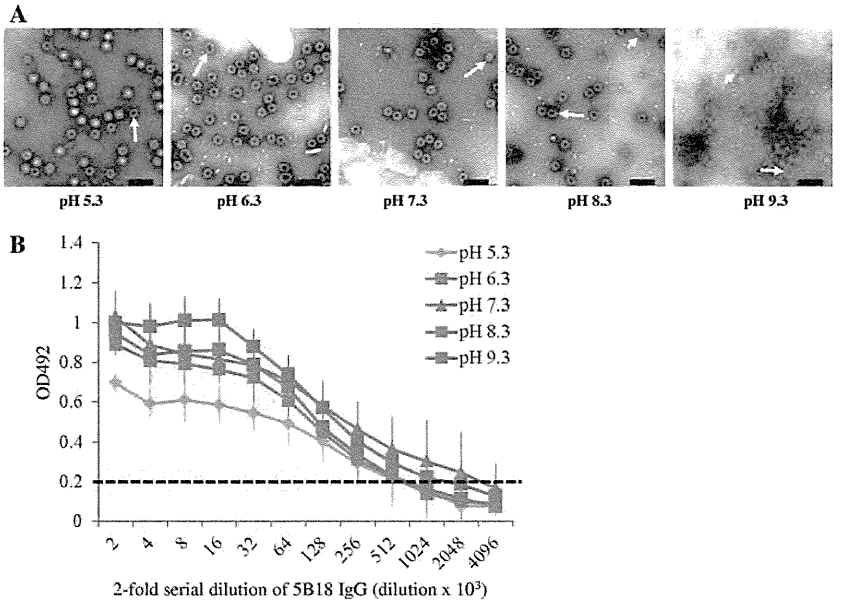

FIG 6 An antibody ELISA was used to determine the binding ability of IgG to GII.10 VLPs. (A) The morphology of the VLPs was examined using EM. At low pHs (from pH 5.3 to 7.3), the majority of the VLPs appeared intact, while above pH 7.3, many of the VLPs appeared broken (long arrows). Small VLPs were also found (short arrows). Scale bar, 100 nm. (B) The same VLPs shown in panel A were used in an ELISA to compare the binding ability of 5B18 IgG. The OD values represent the means of the results for 4 wells; error bars are shown. The OD at 492 nm (OD492) was determined; the dashed line shows the OD492 cutoff of 0.2 (21). The 5B18 IgG detected GII.10 VLPs at different pH values. At pH 7.3, the titer was 2,048,000, while the titers of the other pH values were 2- or 4-fold lower, indicating similar cross-reactivities.

P domains out of the conformation observed in the cryo-EM reconstruction and breaking the P1-P1 domain contacts seen in the VLP. This may be possible since the S domain-P1 subdomain connection in GII noroviruses is particularly long and flexible.

The structural differences between the GI.1 and GII.10 norovirus VLPs do not appear to be a consequence of sequence diversity, since the GI.1 and GII.4 VLP structures are similar and distinct from the GV.1 virion and GII.10 VLP structures. Moreover, the VLP preparation and cryo-EM techniques appear to be essentially the same (54). Two factors that may have affected the particle structures were the insect cell type and the pH of the VLPs. The GI.1 VLPs were expressed in *Spodoptera frugiperda* (Sf9) cells, purified by CsCl ultracentrifugation, and then resuspended in water (pH not described in text) (53, 54), and the GII.10 VLPs were expressed in *Trichopulsia ni* (H5) cells, purified by CsCl ultracentrifugation, and then resuspended in PBS (pH 7.3). We note parenthetically that the cryo-EM structures of hepatitis E virus VLPs expressed in Sf9 and H5 cells are similar, although the processing of the viral protein appeared different (38). Our EM results showed that GII.10 VLPs were intact particles at pH 5.3, 6.3, and 7.3, while another study found that the diameter of norovirus VLPs remained virtually unchanged at pH 3 to 7 but appeared smaller at pH 8 (2). This suggests that the insect cell line and water/PBS (neutral pH) did not affect the overall structure of the VLPs. However, another study has shown that a pH change from 7.6 to 5.0 could cause large structural changes in *Nudaurelia capensis* ω virus VLPs (43, 62). It is possible that these varied conformations do not represent different, stable norovirus structures but are rather all part of a wide spectrum of conformations afforded by the flexible tether between the P and S domains. From previous studies (30), it is clear that this "floating P domain" conformation is independent of whether the sample is a VLP or infectious virion. Since this extended conformation is now observed in rabbit hemorrhagic disease virus (also a calicivirus, genus *Lagovirus*), it also cannot be dependent upon calicivirus genera. It is possible that the energy differences between the conformations represented by these viruses is relatively small and that subtle protein-protein interaction differences favor one conformation under particular conditions. It would be particularly interesting to examine the conformations of these viruses under a broad range of conditions that mimic the expected environments during the viral life cycle. Such changes in virion structure have been observed with numerous other viruses (3, 9, 46, 64, 71). In the case of GV.1 norovirus, where there is an animal model (69) and infectious clone (66), it would also be important to determine what role this flexible tether region has in the replication of the virions and pathology of the disease.

It is important to note that the observed ELISA binding of 5B18 IgG may not occur with intact VLPs. It is possible that denatured or partially broken VLPs or the presence of contaminating GII.10 VP1 was responsible for the binding observed in the ELISA (19, 20, 24). However, it is known that high pH (8.3 or above), partially breaks or denatures norovirus VLPs (2). Despite this pH dependence, the titer remained almost identical, especially in the comparison between pHs 7.3 to 9.3 (Fig. 6), suggesting that only intact or structurally stable virions are being detected. Moreover, the 5B18 antibody could detect GII.10 VLPs that were bound to the plates via histo-blood group antigens, which required a dimeric interaction (22; also unpublished data). Finally three other antibodies, MAb14-1 and NV3901/NV3912, which bound in close

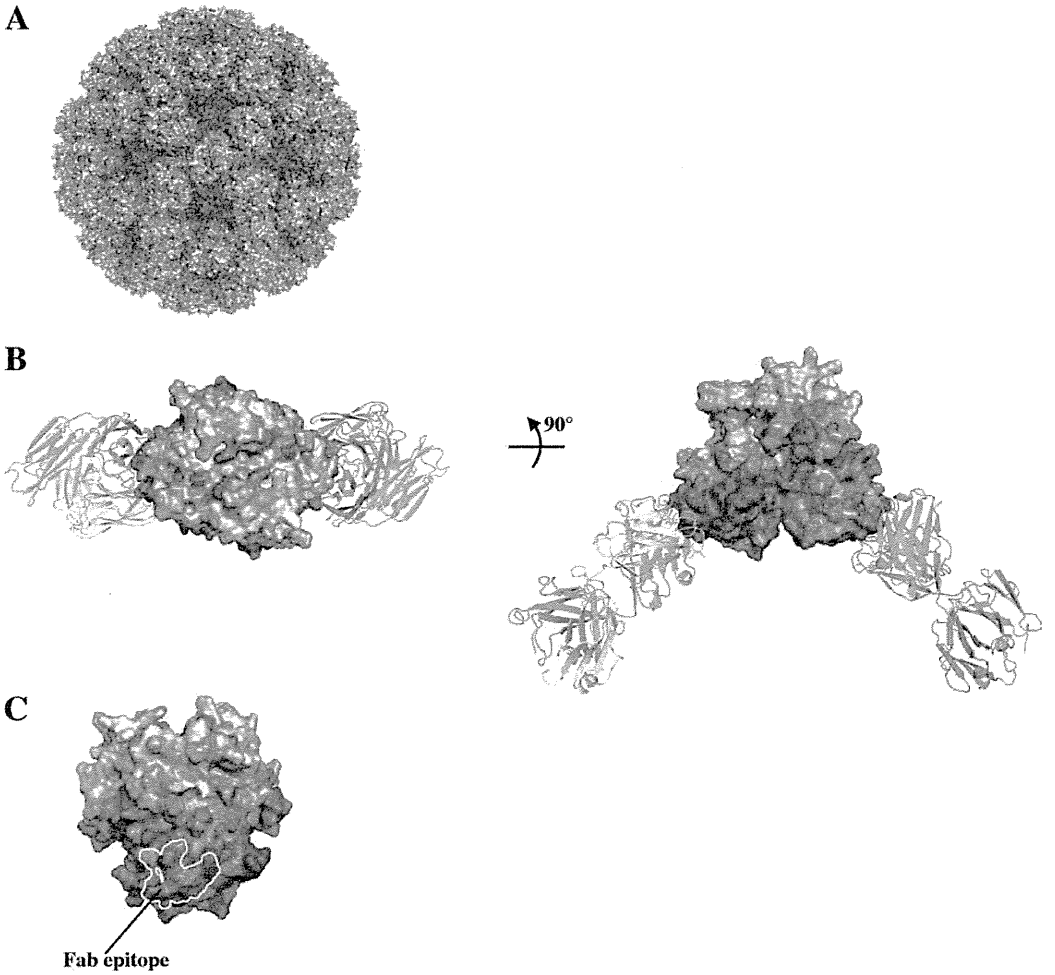

FIG 7 Surface representations of GII amino acid conservation. Noroviruses are genetically and antigenically distinct, with the S domain being more conserved than the P domain. (A) The GII amino acid variability was mapped onto the model of the GII.10 VLP (GI.1 S domain and GII.10 P domain). Amino acid conservation ranges are color-coded from deep purple (highly conserved) to white (highly variable). (B) The amino acid variability was mapped onto the GII.10 P domain apo structure (3ONU) with the 5B18 Fab bound. The top of the P domain was highly variable (left side), while the bottom half of the P domain was more conserved (right side). (C) The Fab binding footprint was mapped onto the P domain (yellow line). The footprint was at a highly conserved area on the wall of the P domain (inside the particle).

proximity to the 5B18 were all shown to detect VLPs (50, 59). These data therefore favor a model in which apparently intact norovirus capsids can indeed bind the 5B18 antibody (and other antibodies) despite significant steric clashes with the VLP structure.

Viruses often use remarkable conformational changes in their envelope or capsid structures to protect their genetic material by waiting for the proper cellular trigger to release their genome into the host cell. For example, the hemagglutinin spike in influenza undergoes a drastic pH-dependent conformational change in the endosome that initiates membrane fusion (8, 68). Similarly large pH-dependent changes have been observed with the enveloped flaviviruses (31, 32, 47) and alphaviruses (36, 45). Such changes due to environmental cues can expose or hide antigenic sites (e.g., see references 41, 45, and 47). Viruses can also receive cues via interactions with cellular receptors, as is the case with human rhinovirus (25, 26, 48). Viruses also undergo small, dynamic structural changes, "breathing" (6, 35, 37, 56), that are probably a prelude to the far larger conformational changes that occur during uncoating. These dynamic motions can transiently expose more-conserved antigenic sites that can be leveraged in designing vaccines (29, 37). However, the fact that these norovirus antibodies are recognizing deeply occluded portions of the P1 domain in apparently intact virions represents a different kind of viral dynamic: for this recognition to occur, the P domains must be capable of extremely large conformational changes without any obvious environmental cue. Such recognition would probably involve just one or a few P domains of a VLP being recognized by antibody 5B18; indeed, images of VLPs after incubation with an excess of antibody 5B18 for 1 h at 37°C (the same incubation used in the ELISA) shows them to be intact, with bound IgG difficult to detect (see Fig. S7 in the supplemental material).

Other antibodies have recently been described that bind to occluded sites on virions. With West Nile virus, the fusion loop-specific antibody E53 recognizes an epitope that should be inaccessible on mature virions. However, this antibody could neutralize mature West Nile virus in a time- and temperature-dependent manner, indicating a role of virus "breathing" or conformational dynamics in antibody recognition (17). With HIV-1, broadly neutralizing antibodies against the membrane-proximal external region of the virus do not appear to recognize the native viral spike (11, 58), again implicating conformational rearrangements to permit antibody recognition. These studies, along with the present study on norovirus recognition by 5B18, suggest substantial flexibility in certain virus particles as being important biologically for antibody-mediated recognition.

In summary, we have shown that a broadly reactive monoclonal antibody binds to an occluded site on the GII.10 P1 subdomain. The binding site was in close proximity to other monoclonal antibody binding sites, suggesting that the site contained an immunodominant region. We also found that the GII.10 VLP structure was more closely related to a GV.1 virion structure than to a GI.1 VLP structure and has marked flexibility in the P domains. These studies suggest that the P domain of noroviruses is capable of adopting variable conformations with respect to the S domain. Despite the vaunted diversity of noroviruses, especially on the exposed outer surface of the virion, one mechanism to achieve near pan-recognition by antibody may be to target a highly conserved domain interface that is dynamically exposed to the environment.

ACKNOWLEDGMENTS

We thank J. Stuckey for assistance with figures and members of the Structural Biology Section at the NIH Vaccine Research Center for help with Fab preparation and comments on the manuscript, K. Nagayama for generous help and insightful discussions, and M. Kataoka for assistance with electron microscopy.

G.S.H. and P.D.K. conceived the project; G.S.H. performed X-ray crystallography and biochemical assays with assistance from J.S.M., S.-Y.P., and P.D.K.; D.W.T. determined the cryo-EM structure with assistance from K.M.; M.Y., F.G., M.M., and K.K. provided the 5B18 IgG; I.G. mapped sequence conservation onto the GII.10 VLP; and G.S.H., D.W.T., J.S.M., T.J.S., I.G., J.R.H.T., K.M., and P.D.K. analyzed the data and wrote the paper, on which all authors commented.

Support for this work was provided by the Intramural Research Program of the National Institutes of Health (NIAID [P.D.K.]), USA, and by a Grant-in-Aid for Scientific Research, grants from the Ministry of Health, Labor, and Welfare of Japan, and a grant from the National Institute of Natural Sciences (NINS), Japan (K.M.). D.W.T is an NSF Graduate Research Fellow and performed this work in Japan as a JSPS/NSF East Asia and Pacific Summer Institute Fellow. Use of Sector 22 (Southeast Region Collaborative Access team) at the Advanced Photon Source was supported by the U.S. Department of Energy, Basic Energy Sciences, Office of Science, under contract no. W-31-109-Eng-38.

REFERENCES

1. **Adams PD, et al.** 2010. PHENIX: a comprehensive Python-based system for macromolecular structure solution. Acta Crystallogr. D. Biol. Crystallogr. 66(Pt 2):213–221.
2. **Ausar SF, Foubert TR, Hudson MH, Vedvick TS, Middaugh CR.** 2006. Conformational stability and disassembly of Norwalk virus-like particles. Effect of pH and temperature. J. Biol. Chem. 281:19478–19488.
3. **Belnap DM, et al.** 2000. Molecular tectonic model of virus structural transitions: the putative cell entry states of poliovirus. J. Virol. 74:1342–1354.
4. **Bhella D, Gatherer D, Chaudhry Y, Pink R, Goodfellow IG.** 2008. Structural insights into calicivirus attachment and uncoating. J. Virol. 82:8051–8058.
5. **Bhella D, Goodfellow IG.** 2011. The cryo-electron microscopy structure of feline calicivirus bound to junctional adhesion molecule A at 9-angstrom resolution reveals receptor-induced flexibility and two distinct conformational changes in the capsid protein VP1. J. Virol. 85: 11381–11390.
6. **Bothner B, Dong XF, Bibbs L, Johnson JE, Siuzdak G.** 1998. Evidence of viral capsid dynamics using limited proteolysis and mass spectrometry. J. Biol. Chem. 273:673–676.
7. **Bu W, et al.** 2008. Structural basis for the receptor binding specificity of Norwalk virus. J. Virol. 82:5340–5347.
8. **Bullough PA, Hughson FM, Skehel JJ, Wiley DC.** 1994. Structure of influenza haemagglutinin at the pH of membrane fusion. Nature 371: 37–43.
9. **Canady MA, Tihova M, Hanzlik TN, Johnson JE, Yeager M.** 2000. Large conformational changes in the maturation of a simple RNA virus, nudaurelia capensis omega virus (NomegaV). J. Mol. Biol. 299:573–584.
10. **Cao S, et al.** 2007. Structural basis for the recognition of blood group trisaccharides by norovirus. J. Virol. 81:5949–5957.
11. **Chakrabarti BK, et al.** 2011. Direct antibody access to the HIV-1 membrane-proximal external region positively correlates with neutralization sensitivity. J. Virol. 85:8217–8226.
12. **Chen R, et al.** 2004. Inter- and intragenus structural variations in caliciviruses and their functional implications. J. Virol. 78:6469–6479.
13. **Choi JM, Hutson AM, Estes MK, Prasad BV.** 2008. Atomic resolution structural characterization of recognition of histo-blood group antigens by Norwalk virus. Proc. Natl. Acad. Sci. U. S. A. 105:9175–9180.
14. **Collaborative Computational Project N.** 1994. The CCP4 suite: programs for protein crystallography. Acta Crystallogr. D. Biol. Crystallogr. 50:760–763.
15. **de Bruin E, Duizer E, Vennema H, Koopmans MP.** 2006. Diagnosis of Norovirus outbreaks by commercial ELISA or RT-PCR. J. Virol. Methods 137:259–264.
16. **Dolinsky TJ, Nielsen JE, McCammon JA, Baker NA.** 2004. PDB2PQR: an automated pipeline for the setup of Poisson-Boltzmann electrostatics calculations. Nucleic Acids Res. 32:W665–W667.
17. **Dowd KA, Jost CA, Durbin AP, Whitehead SS, Pierson TC.** 2011. A dynamic landscape for antibody binding modulates antibody-mediated neutralization of West Nile virus. PLoS Pathog. 7:e1002111.
18. **Emsley P, Lohkamp B, Scott WG, Cowtan K.** 2010. Features and development of COOT. Acta Crystallogr. D. Biol. Crystallogr. 66:486–501.
19. **Graham DY, et al.** 1994. Norwalk virus infection of volunteers: new insights based on improved assays. J. Infect. Dis. 170:34–43.
20. **Greenberg HB, et al.** 1981. Proteins of Norwalk virus. J. Virol. 37:994–999.
21. **Hansman GS, et al.** 2006. Genetic and antigenic diversity among noroviruses. J. Gen. Virol. 87:909–919.
22. **Hansman GS, et al.** 2011. Crystal structures of GII.10 and GII.12 norovirus protruding domains in complex with histo-blood group antigens reveal details for a potential site of vulnerability. J. Virol. 85:6687–6701.
23. **Hansman GS, et al.** 2004. Detection of norovirus and sapovirus infection among children with gastroenteritis in Ho Chi Minh City, Vietnam. Arch. Virol. 149:1673–1688.
24. **Hardy ME, White LJ, Ball JM, Estes MK.** 1995. Specific proteolytic cleavage of recombinant Norwalk virus capsid protein. J. Virol. 69:1693–1698.
25. **Hewat EA, Blaas D.** 2004. Cryoelectron microscopy analysis of the structural changes associated with human rhinovirus type 14 uncoating. J. Virol. 78:2935–2942.
26. **Hoover-Litty H, Greve JM.** 1993. Formation of rhinovirus-soluble ICAM-1 complexes and conformational changes in the virion. J. Virol. 67:390–397.
27. **Jiang X, Wang M, Graham DY, Estes MK.** 1992. Expression, self-assembly, and antigenicity of the Norwalk virus capsid protein. J. Virol. 66:6527–6532.
28. **Kamata K, et al.** 2005. Expression and antigenicity of virus-like particles of norovirus and their application for detection of noroviruses in stool samples. J. Med. Virol. 76:129–136.
29. **Katpally U, Fu T, Freed DC, Casimiro DR, Smith TJ.** 2009. Antibodies to the buried N-terminus of rhinovirus VP4 exhibit cross-serotypic neutralization. J. Virol. 83:7040–7048.

30. **Katpally U, et al.** 2010. High-resolution cryo-electron microscopy structures of murine norovirus 1 and rabbit hemorrhagic disease virus reveal marked flexibility in the receptor binding domains. J. Virol. **84**:5836–5841.
31. **Kaufmann B, et al.** 2009. Capturing a flavivirus pre-fusion intermediate. PLoS Pathog. **5**:e1000672.
32. **Kaufmann B, et al.** 2006. West Nile virus in complex with the Fab fragment of a neutralizing monoclonal antibody. Proc. Natl. Acad. Sci. U. S. A. **103**:12400–12404.
33. **Krissinel E, Henrick K.** 2007. Inference of macromolecular assemblies from crystalline state. J. Mol. Biol. **372**:774–797.
34. **Kwong PD, et al.** 1999. Probability analysis of variational crystallization and its application to gp120, the exterior envelope glycoprotein of type 1 human immunodeficiency virus (HIV-1). J. Biol. Chem. **274**:4115–4123.
35. **Lewis JK, Bothner B, Smith TJ, Siuzdak G.** 1998. Antiviral agent blocks breathing of the common cold virus. Proc. Natl. Acad. Sci. U. S. A. **95**: 6774–6778.
36. **Li L, Jose J, Xiang Y, Kuhn RJ, Rossmann MG.** 2010. Structural changes of envelope proteins during alphavirus fusion. Nature **468**:705–708.
37. **Li Q, Yafal AG, Lee YMH, Hogle J, Chow M.** 1994. Poliovirus neutralization by antibodies to internal epitopes of VP4 and VP1 results from reversible exposure of the sequences at physiological temperatures. J. Virol. **68**:3965–3970.
38. **Li TC, et al.** 2005. Essential elements of the capsid protein for self-assembly into empty virus-like particles of hepatitis E virus. J. Virol. **79**: 12999–13006.
39. **Li X, Zhou R, Tian X, Li H, Zhou Z.** 2010. Characterization of a cross-reactive monoclonal antibody against Norovirus genogroups I, II, III and V. Virus Res. **151**:142–147.
40. **Lochridge VP, Jutila KL, Graff JW, Hardy ME.** 2005. Epitopes in the P2 domain of norovirus VP1 recognized by monoclonal antibodies that block cell interactions. J. Gen. Virol. **86**:2799–2806.
41. **Lok S-M, et al.** 2008. Binding of a neutralizing antibody to dengue virus alters the arrangement of surface glycoproteins. Nat. Struct. Mol. Biol. **15**:312–317.
42. **Majeed S, et al.** 2003. Enhancing protein crystallization through precipitant synergy. Structure **11**:1061–1070.
43. **Matsui T, Lander G, Johnson JE.** 2009. Characterization of large conformational changes and autoproteolysis in the maturation of a T=4 virus capsid. J. Virol. **83**:1126–1134.
44. **McCoy AJ, et al.** 2007. Phaser crystallographic software. J. Appl. Crystallogr. **40**:658–674.
45. **Meyer WJ, Gidwitz S, Ayers VK, Schoepp RJ, Johnston RE.** 1992. Conformational alteration of Sindbis virion glycoproteins induced by heat, reducing agents, or low pH. J. Virol. **66**:3504–3513.
46. **Miao Y, Johnson JE, Ortoleva PJ.** 2010. All-atom multiscale simulation of cowpea chlorotic mottle virus capsid swelling. J. Phys. Chem. B. **114**: 11181–11195.
47. **Modis Y, Ogata S, Clements D, Harrison SC.** 2004. Structure of the dengue virus envelope protein after membrane fusion. Nature **427**:313–319.
48. **Olson NH, et al.** 1993. Structure of a human rhinovirus complexed with its receptor molecule. Proc. Natl. Acad. Sci. U. S. A. **90**:507–511.
49. **Otwinowski Z, Minor W.** 1997. Processing of X-ray diffraction data collected in oscillation mode. Methods Enzymol. **276**:307–326.
50. **Parker TD, Kitamoto N, Tanaka T, Hutson AM, Estes MK.** 2005. Identification of genogroup I and genogroup II broadly reactive epitopes on the norovirus capsid. J. Virol. **79**:7402–7409.
51. **Pei J, Grishin NV.** 2001. AL2CO: calculation of positional conservation in a protein sequence alignment. Bioinformatics **17**:700–712.
52. **Pettersen EF, et al.** 2004. UCSF Chimera—a visualization system for exploratory research and analysis. J. Comput. Chem. **25**:1605–1612.
53. **Prasad BV, et al.** 1999. X-ray crystallographic structure of the Norwalk virus capsid. Science **286**:287–290.
54. **Prasad BV, Rothnagel R, Jiang X, Estes MK.** 1994. Three-dimensional structure of baculovirus-expressed Norwalk virus capsids. J. Virol. **68**: 5117–5125.
55. **Rabenau HF, et al.** 2003. Laboratory diagnosis of norovirus: which method is the best? Intervirology **46**:232–238.
56. **Reisdorph N, et al.** 2003. Human rhinovirus capsid dynamics is controlled by canyon flexibility. Virology **314**:34–44.
57. **Richards AF, et al.** 2003. Evaluation of a commercial ELISA for detecting Norwalk-like virus antigen in faeces. J. Clin. Virol. **26**:109–115.
58. **Ruprecht CR, et al.** 2011. MPER-specific antibodies induce gp120 shedding and irreversibly neutralize HIV-1. J. Exp. Med. **208**:439–454.
59. **Shiota T, et al.** 2007. Characterization of a broadly reactive monoclonal antibody against norovirus genogroups I and II: recognition of a novel conformational epitope. J. Virol. **81**:12298–12306.
60. **Tan M, Hegde RS, Jiang X.** 2004. The P domain of norovirus capsid protein forms dimer and binds to histo-blood group antigen receptors. J. Virol. **78**:6233–6242.
61. **Tang G, et al.** 2007. EMAN2: an extensible image processing suite for electron microscopy. J. Struct. Biol. **157**:38–46.
62. **Tang J, et al.** 2009. Dynamics and stability in maturation of a T=4 virus. J. Mol. Biol. **392**:803–812.
63. **Taube S, et al.** 2010. High-resolution X-ray structure and functional analysis of the murine norovirus 1 capsid protein protruding domain. J. Virol. **84**:5695–5705.
64. **Trus BL, et al.** 1996. The herpes simplex virus procapsid: structure, conformational changes upon maturation, and roles of the triplex proteins VP19c and VP23 in assembly. J. Mol. Biol. **263**:447–462.
65. **van Heel M, Harauz G, Orlova EV, Schmidt R, Schatz M.** 1996. A new generation of the IMAGIC image processing system. J. Struct. Biol. **116**: 17–24.
66. **Ward VK, et al.** 2007. Recovery of infectious murine norovirus using pol II-driven expression of full-length cDNA. Proc. Natl. Acad. Sci. U. S. A. **104**:11050–11055.
67. **Widdowson M-A, et al.** 2005. Detection of serum antibodies to bovine norovirus in veterinarians and the general population in the Netherlands. J. Med. Virol. **76**:119–128.
68. **Wilson IA, Skehel JJ, Wiley DC.** 1981. Structure of the haemagglutinin membrane glycoprotein of influenza virus at 3Å resolution. Nature **289**: 366–373.
69. **Wobus CE, Thackray LB, Virgin HW.** 2006. Murine norovirus: a model system to study norovirus biology and pathogenesis. J. Virol. **80**:5104–5112.
70. **Yoda T, et al.** 2003. Precise characterization of norovirus (Norwalk-like virus)-specific monoclonal antibodies with broad reactivity. J. Clin. Microbiol. **41**:2367–2371.
71. **Yu IM, et al.** 2008. Structure of the immature dengue virus at low pH primes proteolytic maturation. Science **319**:1834–1837.
72. **Zheng DP, et al.** 2006. Norovirus classification and proposed strain nomenclature. Virology **346**:312–323.

Molecular Cell
Article

The Kelch Repeat Protein KLHDC10 Regulates Oxidative Stress-Induced ASK1 Activation by Suppressing PP5

Yusuke Sekine,[1] Ryo Hatanaka,[1] Takeshi Watanabe,[1] Naoki Sono,[1] Shun-ichiro Iemura,[3,5] Tohru Natsume,[3] Erina Kuranaga,[2,4] Masayuki Miura,[2] Kohsuke Takeda,[1,6] and Hidenori Ichijo[1,*]
[1]Laboratory of Cell Signaling
[2]Department of Genetics
Graduate School of Pharmaceutical Sciences, The University of Tokyo, 7-3-1 Hongo, Bunkyo-ku, Tokyo 113-0033, Japan
[3]Biological Systems Control Team, Biomedicinal Information Research Center, National Institutes of Advanced Industrial Science and Technology, 2-42 Aomi, Koto-ku, Tokyo 135-0064, Japan
[4]Laboratory for Histogenetic Dynamics, RIKEN Center for Developmental Biology, 2-2-3 Minatojima-minamimachi, Chuo-ku, Kobe 650-0047, Japan
[5]Present address: Division of Translational Research for Drug Development, Fukushima Medical University, 1 Hikariga-oka, Fukushima-shi, Fukushima 960-1295, Japan
[6]Present address: Division of Cell Regulation, Graduate School of Biomedical Sciences, Nagasaki University, 1-14 Bunkyo-machi, Nagasaki 852-8521, Japan
*Correspondence: ichijo@mol.f.u-tokyo.ac.jp
http://dx.doi.org/10.1016/j.molcel.2012.09.018

SUMMARY

Reactive oxygen species (ROS)-induced activation of Apoptosis signal-regulating kinase 1 (ASK1) plays crucial roles in oxidative stress-mediated cell death through the activation of the JNK and p38 MAPK pathways. However, the regulatory mechanism of ASK1 in the oxidative stress response remains to be elucidated. Here, we identified the kelch repeat protein, Slim, as an activator of ASK1 through a *Drosophila* misexpression screen. We also performed a proteomics screen and revealed that Kelch domain containing 10 (KLHDC10), a mammalian ortholog of Slim, interacted with Protein phosphatase 5 (PP5), which has been shown to inactivate ASK1 in response to ROS. KLHDC10 bound to the phosphatase domain of PP5 and suppressed its phosphatase activity. Moreover, KLHDC10 was required for H_2O_2-induced sustained activation of ASK1 and cell death in Neuro2A cells. These findings suggest that Slim/KLHDC10 is an activator of ASK1, contributing to oxidative stress-induced cell death through the suppression of PP5.

INTRODUCTION

During the process of aerobic metabolism in cells, reactive oxygen species (ROS), such as superoxide anions, hydrogen peroxide (H_2O_2), and hydroxyl radicals, are produced by intracellular enzymatic systems, including the mitochondrial electron transport chain. Stressors from the exogenous environment, such as ultraviolet radiation, ionizing radiation, and anticancer drugs, also cause the formation of ROS. Excessive and/or ectopic generation of ROS results in oxidative stress, in which ROS induce nonspecific oxidation of nucleic acids, lipids, and proteins, leading to profound damage to the cells and eventually cell death. Accordingly, ROS have been considered to be the cause of various human diseases and aging. To cope with oxidative stress and maintain the intracellular homeostasis of redox status, living organisms are equipped with a wide variety of antioxidant proteins and redox-sensitive signaling systems (Finkel and Holbrook, 2000).

The mitogen-activated protein kinase (MAPK) cascades are evolutionarily conserved signaling pathways that play crucial roles in cellular responses to environmental changes (Kyriakis and Avruch, 2001; Widmann et al., 1999). Apoptosis signal-regulating kinase 1 (ASK1) is a member of the MAP kinase kinase kinases (MAP3K) that activates the c-Jun N-terminal kinase (JNK) and p38 MAPK pathways in response to a wide variety of pathophysiological stressors, including oxidative stress, endoplasmic reticulum (ER) stress, and inflammatory cytokines (Ichijo et al., 1997; Takeda et al., 2008). ASK1 has been demonstrated to be involved in ROS-induced cell death in various types of cells and has been implicated in the pathogenesis of oxidative stress-related diseases such as neurodegenerative diseases, cardiovascular diseases, and cancers (Nagai et al., 2007; Tobiume et al., 2001). The molecular mechanism of ASK1 activation by ROS has been revealed mainly through analyzing ASK1-binding proteins. Under conditions in which there is no oxidative stress, the antioxidant protein thioredoxin (Trx) forms a complex with ASK1 through the N-terminal region of ASK1, and inhibits ASK1's kinase activity (Saitoh et al., 1998). Under oxidative stress conditions, the reactive cysteine residues within Trx are oxidized and form an intramolecular disulfide bond. The oxidized form of Trx is released from ASK1, and reciprocally tumor necrosis factor (TNF) receptor-associated factor (TRAF) family proteins, such as TRAF2 and TRAF6, are recruited to ASK1 (Fujino et al., 2007; Nishitoh et al., 1998; Noguchi et al., 2005). The interaction of TRAFs with ASK1 appears to enhance

the transautophosphorylation of the threonine residue within the activation loop of the kinase domain of ASK1, which is essential for ASK1 activation (Nishitoh et al., 1998). Although Trx and TRAF family proteins are pivotal molecules in the regulation of ROS-induced activation of ASK1, we have also demonstrated that Protein phosphatase 5 (PP5) is a negative regulator of ASK1 (Morita et al., 2001). PP5 is a serine/threonine phosphatase that belongs to the Phosphoprotein phosphatase (PPP) family. It has been reported that PP5 is involved in hormone and stress responses by dephosphorylating various substrates (Golden et al., 2008; Hinds and Sánchez, 2008). PP5 interacts with the activated form of ASK1 in response to H_2O_2 and dephosphorylates the essential phosphothreonine residue, thereby inhibiting the kinase activity of ASK1 and oxidative stress- and ASK1-dependent apoptosis. Thus, PP5 is one of the key molecules that determine the cell fate in the oxidative stress response.

The kelch repeat domain consists of five to seven tandem repeats of the kelch motif and forms a β-propeller structure (Adams et al., 2000; Prag and Adams, 2003). The kelch repeat protein family members exist across species and have been reported to play roles in a wide range of cellular processes, including signal transduction, transcription, DNA repair, and protein degradation. Because the kelch repeat domain is important for protein-protein interactions, the kelch repeat proteins function mainly through interaction with their binding partners. Recently, several lines of evidence have demonstrated that the kelch repeat proteins interact with the complex-type ubiquitin E3 ligases called the Cullin-RING ligases (CRLs) and serve as the substrate recognition subunits of the CRL complex, which determine the substrate specificity of this complex (Bennett et al., 2010). However, the molecular functions and physiological roles of most kelch repeat proteins remain unknown.

Here, we identified the kelch repeat protein Slim and its mammalian ortholog KLHDC10 as an activator of ASK1 by taking advantage of *Drosophila* genetics. Slim/KLHDC10 was found to activate ASK1 through the suppression of PP5 and thereby to contribute to oxidative stress-induced cell death.

RESULTS

A Misexpression Screen for Activators of ASK1 using *Drosophila*

To identify genes that regulate activation of the ASK1-MAPK cascades, we took advantage of a *Drosophila* misexpression screen, using the GAL4/UAS system that has been extensively used to induce ectopic gene expression in flies (Brand and Perrimon, 1993). We have recently reported that an N terminus-lacking mutant of *Drosophila* ASK1 (DASK1 ΔN) activated the *Drosophila* p38 (Dp38) pathway more strongly than did DASK1 wild-type (WT) (Sekine et al., 2011). Ectopic expression of DASK1 ΔN, but not DASK1 WT, under the control of *pannier* (*pnr*)-*GAL4*, which is expressed along the dorsal midline of adult flies, resulted in a Dp38-dependent increase in melanization (increase in black and brown pigments) in the thorax cuticle of flies (Figures 1A and 1B) (Sekine et al., 2011). To establish a misexpression screening system for activators of ASK1, we used this melanization as a visible marker for activation of the ASK1-p38 pathway in flies and sought to screen for genes that could induce melanization in the thorax in a *pnr-GAL4*-dependent manner. The Gene Search (GS) lines have a GS vector that contains UAS, which is randomly inserted in the fly genome of each GS line, thereby allowing ectopic expression of endogenous genes after crossing with the GAL4 driver strains (Toba et al., 1999). We generated *pnr > DASK1WT* flies and crossed them with approximately 4,500 GS lines. The melanization of thoraxes of the F1 progeny was examined, and nine lines were found to exhibit enhanced melanization in a *pnr-GAL4*-dependent manner. We designated those lines as *kuma* (*key upswing in melanin accumulation*) lines.

Slim Expression in *pnr > kuma1* Flies Induces Melanization

Of the nine *kuma* lines, we focused on the *kuma1* (GS10238) line. All of the *pnr > kuma1* flies exhibited strong melanization, similar to *pnr > DASK1ΔN*, even without coexpression of DASK1 WT (Figure 1C). These results suggest that *kuma1*-dependent activation of endogenous DASK1-Dp38 may be sufficient to melanize the thorax in these conditions. When we crossed the flies at 18°C (a temperature that weakly induced the gene misexpression in *kuma1*), about half of the *pnr > kuma1* flies showed a weak phenotype that resulted in the loss of the upper half of melanization in the thoracic *pnr-GAL4* expression region (indicated by the white arrowhead in Figure 1D). Under these conditions, coexpression of DASK1 WT restored the melanization in *pnr > kuma1* flies, suggesting that exogenous DASK1 enhanced the melanization in *pnr > kuma1* flies (Figure 1D). The GS vector in the *kuma1* line was inserted 508 bases upstream of a gene, *scruin like at the midline* (*slim*) (Figure 1E), and we examined the expression levels of *slim* in *kuma1* lines under the control of heat shock (hs)-inducible GAL4. The expression of *slim* mRNA in *hs > kuma1* flies was elevated compared to that in *hs > GFP* flies, whereas the expression levels of *DASK1* or *CG5189*, which is located directly 3′ to *slim*, were not affected (Figure 1F). Slim protein levels were also increased in *hs > kuma1* flies (Figure 1G). Furthermore, coexpression of inverted repeat (IR) RNA targeting *slim* (*slim-IR*) strongly reduced the melanization in *pnr > kuma1* flies (Figures 2A and 2B). Based on these results, we concluded that *slim* is the gene responsible for melanization in the thorax of *pnr > kuma1*.

The DASK1-Dp38 Pathway Mediates Slim-Induced Melanization

Because DASK1 ΔN-induced melanization is dependent on the Dp38 pathway (Sekine et al., 2011), we examined the requirement of the DASK1-Dp38 pathway for Slim-induced melanization. IR RNA-mediated knockdown of *DASK1* or *licorne (lic)*, a *Drosophila* MAP2K gene in the Dp38 pathway, in *pnr > kuma1* flies partially inhibited melanization (Figures 2C and 2D). In addition, the expression of a dominant-negative mutant of Dp38a (Dp38a DN) also reduced melanization in *pnr > kuma1* flies (Figure 2E). By contrast, knockdown of *slim* did not affect DASK1 ΔN-induced melanization (Figures 2F and 2G), indicating that *slim* is genetically located upstream of *DASK1* and that Slim-induced melanization was mediated through the DASK1-Dp38 pathway.

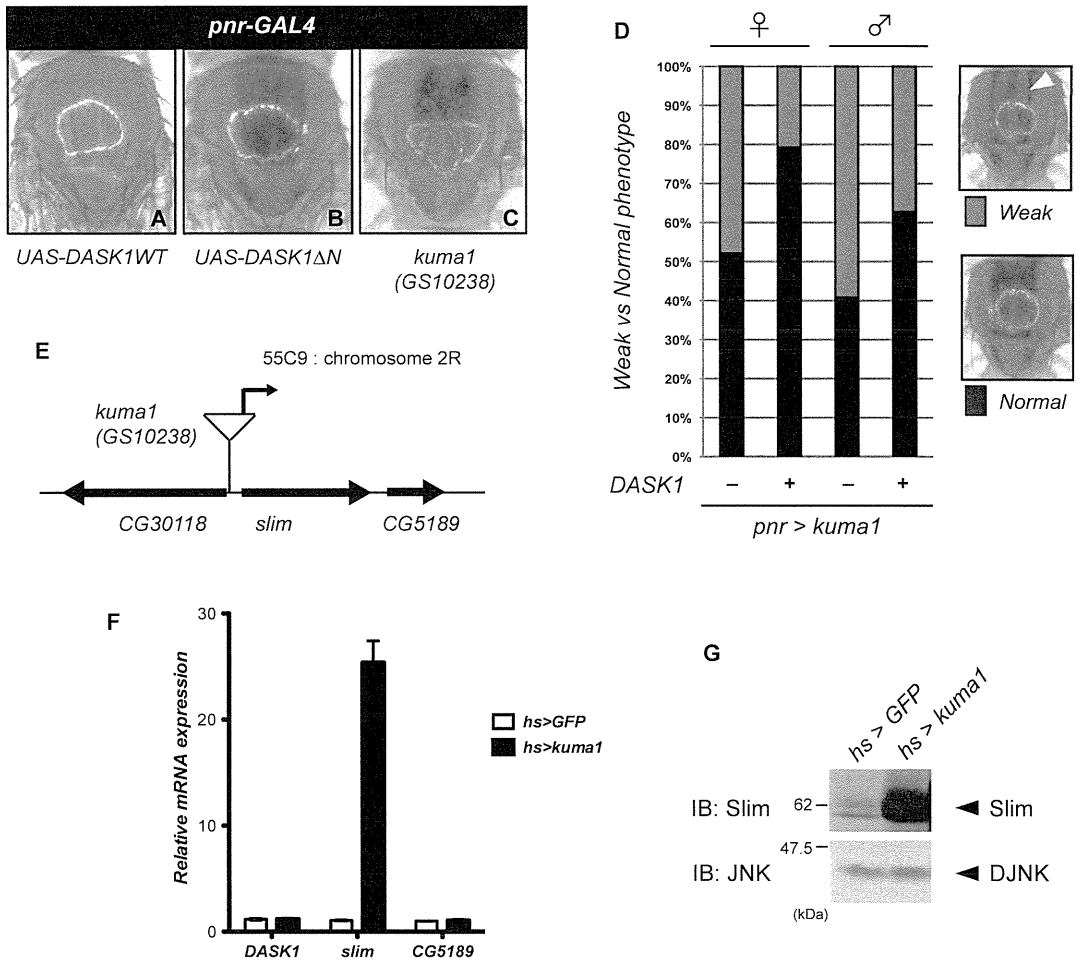

Figure 1. Ectopic Expression of Slim Induces Melanization in the Fly Thorax

(A and B) Thoraxes of *UAS-DASK1WT/+; pnr-GAL4/+* (A) and *UAS-DASK1ΔN/+; pnr-GAL4/+* (B) flies are shown.

(C) The thorax of a *kuma1/+; pnr-GAL4/+* fly is shown.

(D) Flies were crossed and maintained at 18°C. Under these conditions, about half of all flies exhibited weakened melanization (weak), whereas the other half exhibited a similar extent of melanization to flies crossed at 25°C (normal). The number of flies with weak and normal melanization was counted in *kuma1/+; pnr-GAL4/+* flies (48 females and 71 males) and *kuma1/UAS-DASK1WT; pnr-GAL4/+* flies (48 females and 59 males). The white arrowhead indicates reduced melanization in the flies with the weak phenotype.

(E) A schematic representation of the GS vector insertion site within chromosome 2R of the *kuma1* (*GS10238*) line. The GS vector, in which the gene is expressed in the direction of the arrow, was inserted 508 base upstream of the *slim* gene.

(F) Total RNA isolated from the heat-shocked adult flies of *UAS-GFP^{S65T}/hs-GAL4* (*hs > GFP*) and *kuma1/hs-GAL4* (*hs > kuma1*) was analyzed by qRT-PCR analysis for the indicated genes. The results shown are the means of three independent RNA samples. Error bars indicate SEM.

(G) Heat-shocked adult males of *hs > GFP* and *hs > kuma1* were lysed and subjected to immunoblotting (IB).

The Kelch Repeat Protein Slim/KLHDC10 Activates ASK1

To examine whether the expression of Slim indeed activates DASK1, we transfected Flag-tagged Slim and DASK1 into *Drosophila* S2 cells and performed immunoblotting analysis. Activation of DASK1 was monitored using an antibody against the phosphothreonine residue within the kinase domain of ASK1 (Thr838 and Thr747 in human and *Drosophila* ASK1, respectively) that is essential for the activation of the ASK family proteins (Kuranaga et al., 2002; Tobiume et al., 2002). The coexpression of Slim and DASK1 induced the activation of DASK1, *Drosophila* JNK (DJNK), and Dp38 (Figure 3A), suggesting that Slim is an activator of the DASK1-MAPK cascades. In contrast, Slim did not activate coexpressed DASK1 ΔN (see Figure S1A online). This result seems to be consistent with the results showing that DASK1 ΔN by itself efficiently induced melanization in fly thorax (Figure 1B) and that knockdown of *slim* did not affect the DASK1 ΔN-induced melanization (Figure 2G).

Kelch domain containing 10 (KLHDC10) is the mammalian counterpart of Slim. The primary structure of both Slim and